nature neuroscience

Article

https://doi.org/10.1038/s41593-025-02038-6

Allothetic and idiothetic spatial cues control the multiplexed theta phase coding of place cells

Received: 24 September 2024

Accepted: 25 June 2025

Published online: 26 August 2025



Check for updates

Yotaro Sueoka 1,2, Ravikrishnan P. Jayakumar 1,3,4, Manu S. Madhav 1,4,5,6, Francesco Savelli^{2,7}, Noah J. Cowan **3**,4,5 & James J. Knierim **1**,2,5

Theta oscillation is considered a temporal scaffold for hippocampal computations that organizes the activity of spatially tuned cells known as place cells. Late phases of theta support prospective spatial representation via phase 'precession'. In contrast, some studies have hypothesized that early phases of theta may subserve both retrospective spatial representation via phase 'procession' and the encoding of new associations. Here, combining virtual reality, electrophysiology and computational modeling, we provide experimental evidence for such a functionally multiplexed phase code and describe how distinct spatial inputs control its manifestation. Specifically, when rats continuously learned new associations between external landmark (allothetic) cues and self-motion (idiothetic) cues, phase 'precession' remained intact, allowing continuous prediction of future positions. Conversely, phase 'procession' was diminished, matching the putative role in encoding at the early theta phase. This multiplexed phase code may serve as a general circuit logic for alternating different computations at a sub-second scale.

The hippocampus is thought to create an internal, spatial representation of the environment, which supports both flexible spatial learning and episodic memory^{1,2}. This cognitive map is instantiated in part by hippocampal place cells, which form spatial firing fields at specific locations of an environment³⁻⁶. A key feature of place cell firing is its entrainment to the theta rhythm, an approximately 8-Hz oscillation in the local field potential (LFP) that appears during certain behavioral epochs, including locomotion and investigatory behaviors⁷⁻⁹. Place cells fire at progressively earlier phases of the theta rhythm as an animal travels through their firing fields, a type of phase coding known as theta phase precession^{10,11} (Fig. 1a). At the single-cell level, spike timing of place cells relative to the theta rhythm encodes the proportion of the place field traversed¹²⁻¹⁸. At the population level, phase precession is

associated with the formation of a forward theta sequence, where the real-world sequence of place cells is reinstantiated at a compressed temporal scale within a theta cycle 11,19-21. Such sequential firing of place cells gives rise to the representation of the animal's future trajectory and is implicated in spatial decision-making²²⁻²⁵. Phase precession is observed across species, including rodents^{10,11}, bats²⁶ and humans²⁷, suggestive of its universal role in hippocampal computation^{28,29}.

Some studies, however, have called into question whether phase precession could fully account for the theta-modulated activity of place cells. Early studies of phase precession reported that the overall precession structure is not always linear and monotonic but often consists of two lobes at different theta phases, with precession occurring mostly at the late phases of theta 11,30 . Prominent models of hippocampal function

¹Solomon H. Snyder Department of Neuroscience, Johns Hopkins University, Baltimore, MD, USA. ²Zanvyl Krieger Mind/Brain Institute, Johns Hopkins University, Baltimore, MD, USA. 3Department of Mechanical Engineering, Johns Hopkins University, Baltimore, MD, USA. 4Laboratory for Computational Sensing and Robotics, Johns Hopkins University, Baltimore, MD, USA. 5Kavli Neuroscience Discovery Institute, Johns Hopkins University, Baltimore, MD, USA. Present address: School of Biomedical Engineering, University of British Columbia, Vancouver, BC, Canada. Present address: Department of Neuroscience, Developmental and Regenerative Biology, The University of Texas at San Antonio, San Antonio, TX, USA. 🖂 e-mail: jknierim@jhu.edu

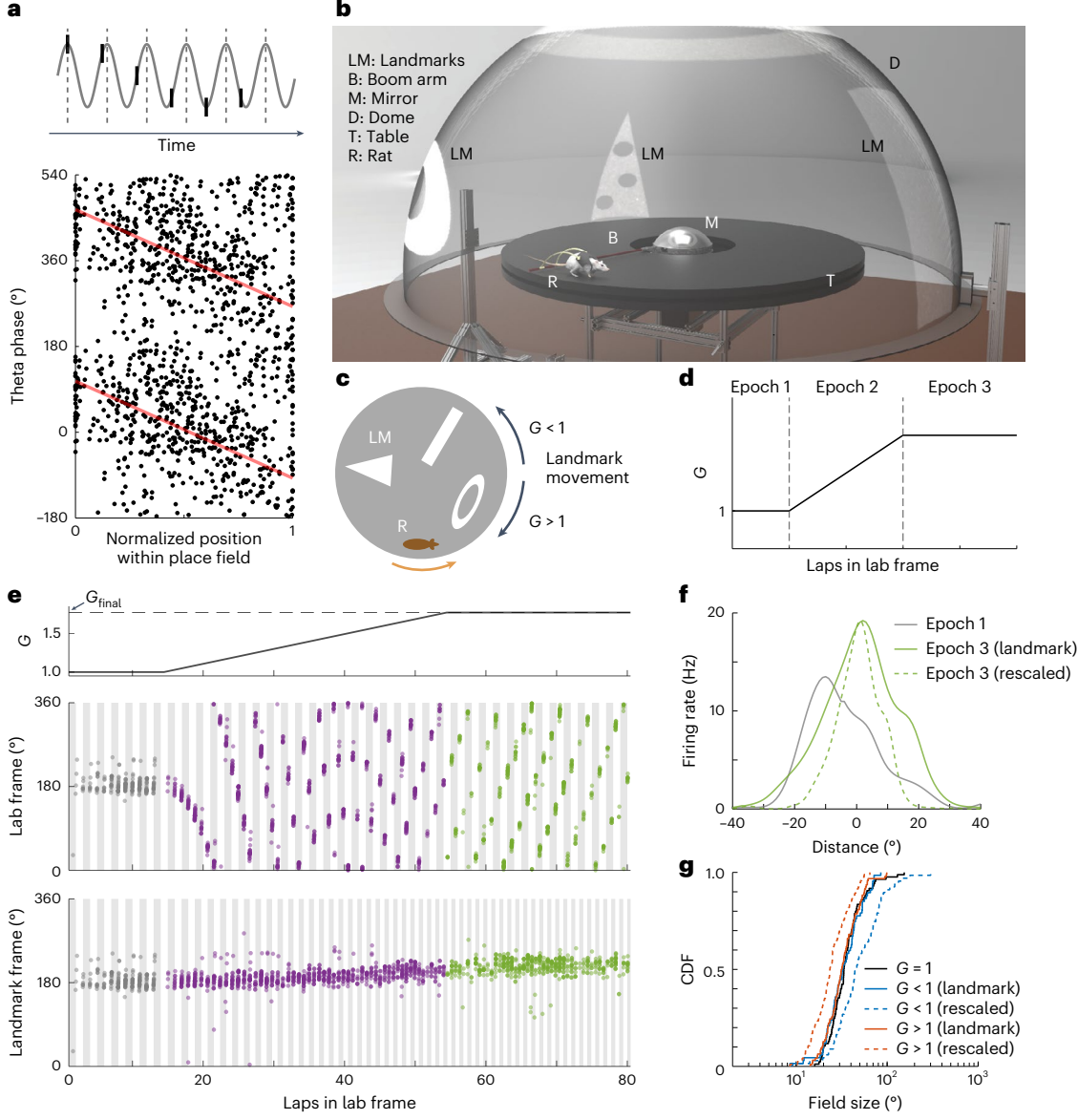


Fig. 1| **Place cells are locked to allothetic spatial cues inside the Dome. a**, Schematic of phase precession. Top: thick vertical ticks represent bursts of spikes along the LFP theta (gray sinusoidal curve). Bottom: dots indicate points in the normalized position—theta phase space where spikes were recorded. The yaxis displays the theta phase repeated for two cycles to better visualize the phase coding structure across the circular phase variable. The red line shows the best-fit circular—linear regression slope to these data. **b**, Semi-transparent illustration of the Dome apparatus. **c**, Illustration of the experimental gain. **d**, Gain dynamics and epoch structure of a typical experimental session. **e**, Representative place cell behavior during an experimental session. Top: profile of experimental gain ($G_{\text{final}} = 1.77$). Middle: dots indicate the positions of the rat on the track (yaxis) where spikes from the unit were recorded in the lab frame. Bottom: same

spikes in the landmark frame. Colors represent spikes from epochs 1–3, and alternate white/gray bars indicate laps in the respective frames. \mathbf{f} , Place fields of the same unit as in \mathbf{e} . In epoch 1, lab frame and landmark frame are identical because G=1. For epoch 3, the place field is plotted in the landmark frame and a calculated lab frame (rescaled) by scaling the place field in the landmark frame by a factor of $1/G_{\text{final}}$. All three fields were aligned by their midpoints. \mathbf{g} , Cumulative density plots (CDFs) of place field sizes. Fields from G<1 and G>1 showed similar distribution as the G=1 condition in the landmark frame ($\beta=0.0249$, s.e. =0.0704, t(243)=0.354, P=0.724 and $\beta=0.100$, s.e. =0.0623, t(243)=1.61, P=0.109, respectively; t-statistics/two-sided P values from the LMEM using the log of field size followed by FDR correction). Rescaled cumulative plots are shown for reference.

have hypothesized that the early phases of theta instead contribute to the encoding of novel information 9.31. This phase range is associated with increased synaptic plasticity 32,33, which can facilitate encoding at individual dendrites without a spiking output 34-36. When an environment is already familiar to the animal, Wang et al. 37 observed prominent phase 'procession' in the early phases of theta, which may allow for retrospective evaluation of ongoing experiences (see also ref. 38). Together, these findings raise the possibility that the early phases of theta may subserve the encoding of new associations or the representation of retrospective spatial location depending on the demand.

In the present study, we directly tested the existence of functional multiplexing within the theta oscillation by systematically controlling the demand to encode new associations between different spatial inputs. External landmarks (allothetic cues) and self-motion (idiothetic) cues serve as the two sources of spatial information that control the activity of place cells³⁹⁻⁴³. Place cell firing is strongly locked to visual landmarks such that place fields can rotate and/or scale in response to corresponding changes to those cues^{14,44-47}. On the other hand, idiothetic cues are used via path integration computations to continually update the animal's location on its cognitive map, both

in the absence and presence of prominent allothetic cues^{39,48,49}. In this study, we created a persistent conflict between these two classes of spatial cues using a planetarium-style, virtual reality system⁵⁰ (the 'Dome') such that animals had to continuously encode a new relationship between the allothetic and idiothetic cues^{47,51}. We found that phase 'precession' remained constant under the cue mismatch. By contrast, phase 'procession' and the spiking activity in the early phases of theta diminished with conflicting allothetic and idiothetic inputs, consistent with switching from representing retrospective trajectories to encoding new associations while suppressing axonal spiking output. Using a continuous attractor network (CAN) model, we demonstrate how conflicting spatial inputs selectively impair phase procession while sparing phase precession. Together, our findings provide experimental support for the multiplexed nature of theta phase coding.

Results

Virtual reality dissociates allothetic and idiothetic spatial cues

To investigate the dissociation of the two modes of phase coding, we recorded the activity of CA1 place cells $(4.74 \pm 3.54 \, (\text{mean} \pm \text{s.d.}) \, \text{units}$ meeting place cell criteria per session; Supplementary Tables 1 and 2) as rats (n = 5) ran around a circular track inside the Dome virtual reality system^{47,50} (Fig. 1b). Rats were tethered to a boom arm attached to a central commutator pillar and ran counterclockwise on the periphery of the table to obtain irregularly spaced liquid rewards. An array of visual landmarks was projected onto the interior of the Dome shell and served as allothetic spatial cues (Methods). To create a persistent conflict between the allothetic and idiothetic spatial cues, the array of landmarks revolved around the center of the environment as a function of the rat's movement. The motion of the visual landmarks was controlled by an experimental gain, G, which specified the ratio of the animal's speed in the landmark frame to its speed in the lab frame. In G > 1 sessions, landmarks moved in the direction opposite to the rat's movement, presumably causing the rat to perceive its motion as faster than it actually was; in G < 1 sessions, landmarks moved in the same direction as the rat, presumably causing the rat to perceive its motion as slower than it actually was (Fig. 1c). Each experimental session started with a G = 1 condition, where the landmarks were stationary (epoch 1; Fig. 1d). The experimental gain value was then linearly ramped up or down (epoch 2) until it reached a target value, G_{final} . In epoch 3, G was held at G_{final} . The Dome apparatus thus gradually introduced a conflict between allothetic spatial cues based on landmarks and idiothetic cues based on self-motion. Most of the analyses focused on epochs 1 and 3, during which G remained constant at the initial value (G=1) and the target value ($G = G_{final}$), respectively.

In 40 of 51 sessions, place fields were stable in the rotating landmark frame (that is, the place fields rotated as a coherent ensemble under the control of the landmarks; see ref. 47 for quantification). Figure 1e shows an example unit from a session with $G_{\text{final}} = 1.77$. In epoch 1, when the landmarks were stationary, the cell fired at the same location in the lab frame (Fig. 1e, middle). Once the landmarks started moving relative to the lab frame (epochs 2 and 3), the firing of the cell was no longer locked to the lab frame. Instead, the place field remained stable in the rotating landmark frame, demonstrating that the place field was strongly controlled by the landmarks, with only a small amount of drift in the firing location over many laps (Fig. 1e, bottom). Compared with the G=1 condition, the rat traversed less distance in the lab frame to complete a full lap in the landmark frame, and, therefore, the physical distance traveled in each pass through the place field (computed by rescaling the distance in landmark frame by the experimental gain) shrunk by a factor of 1/G(1/1.77 = 0.565; Fig. 1f). When all place fields from all sessions were compiled, the distribution of place field sizes was approximately maintained in the landmark frame in G = 1, G > 1 and G < 1 conditions (Fig. 1g) while shrinking or stretching in the lab frame in G > 1 and G < 1 sessions, respectively. Given that the place fields were controlled by the allothetic landmark frame, with no consistent spatial

tuning in the lab frame, we examined how phase coding was affected under the persistent conflict between allothetic and idiothetic cues caused by the experimental gain manipulation.

Theta phase precession is maintained in the landmark frame

To investigate how phase precession was affected by the gain manipulation, we plotted the theta phase of each spike against the normalized position within a place field in the landmark frame. Using a lap-based definition of place fields (Methods), we observed that the phase precession shape exhibited cell-to-cell variability (Fig. 2a), including rare instances (n = 10) of double precessions as was reported previously ^{11,52} (Extended Data Fig. 1). Nonetheless, place cells exhibited phase precessions that were locked to the landmark frame, firing at increasingly earlier phases of LFP theta throughout the field (Fig. 2a). Phase precession plots combining all spiking activities from all place cells further confirmed that phase precession was preserved when G was close to 1 (mid gain: G = 0.7-1.3) as well as when G substantially deviated from 1 (ref. 50) (low gain: G = 0.1-0.7, high gain: G = 1.3-1.9; Fig. 2b). In fact, the slope of the precession, as measured using circular-linear regression⁵³, was invariant across gains in the landmark frame (Fig. 2c). Similarly, the correlation coefficient and phase offset remained constant (Fig. 2d,e). Thus, the precession structure scaled with the distance traveled in the lab frame from the start to the end of the place field 14,54-56. The scaling of precession demonstrates the stronger influence of the allothetic cues relative to the idiothetic cues on the temporal firing pattern of place cells when the hippocampal map is locked to the external landmarks.

Theta-modulated burst frequencies change in response to gain

Under G > 1 and G < 1 conditions, rats had to run shorter or longer physical distances in the lab frame, respectively, to traverse the length of a place field in the landmark frame. We thus investigated how the tem $por al firing \, properties \, of \, place \, cells \, were \, modulated \, to \, maintain \, phase \, and \, properties \, of \, place \, cells \, were \, modulated \, to \, maintain \, phase \, properties \, of \, place \, cells \, properties \, pr$ precession in the landmark frame. Theta phase precessing units fire bursts of spikes at a frequency slightly higher than the LFP theta frequency, and the difference in frequencies correlates with the speed of precession¹⁶ (that is, the change in theta phase of spike bursts between successive theta cycles). In our dataset, LFP theta frequency exhibited session-to-session variability without any apparent relation to gain (Fig. 3a). To quantify the burst frequencies relative to the LFP theta frequencies, we computed the spike phase spectrum^{16,57} (Fig. 3b and Methods). The resulting spectrum would show a peak at a value greater than 1 when the bursting activity contains a prominent precession. The raw precession rate is obtained from the spectrum as the peak frequency – 1, where greater values correspond to faster phase precession. The precession speed is known to be faster in smaller fields compared with larger fields¹⁴ and to increase with the speed of the animal¹⁶. Thus, to isolate the effect of gain on the precession speed, we defined a normalized precession rate (NPR) = (raw precession rate) × (field size in the landmark frame) × (mean theta frequency) / (mean animal speed in the lab frame) (see Methods for details). We found that NPR scaled with gain (Fig. 3c and Extended Data Fig. 2a,b), showing that the theta-modulated bursting frequency adapts to the experimental gain to maintain a constant precession slope in the landmark frame. This scaling in theta-modulated bursting frequency was accompanied by a decrease in the propensity of place cells to skip firing in every other theta cycle (theta skipping $^{24,58-60}$) in the high gain condition compared with mid gain and epoch 1(G=1) conditions (Extended Data Fig. 2c-g).

Theta precession is associated with a population-level phenomenon known as the forward theta sequence. Place cells with partially overlapping fields show differences in the preferred firing phase of LFP theta at any given theta cycle due to phase precession; as a result, the spatial order of place cells with overlapping fields is reinstantiated in a compressed temporal sequence within a theta cycle (Fig. 3d). Given the scaling of theta-modulated bursting frequency and theta

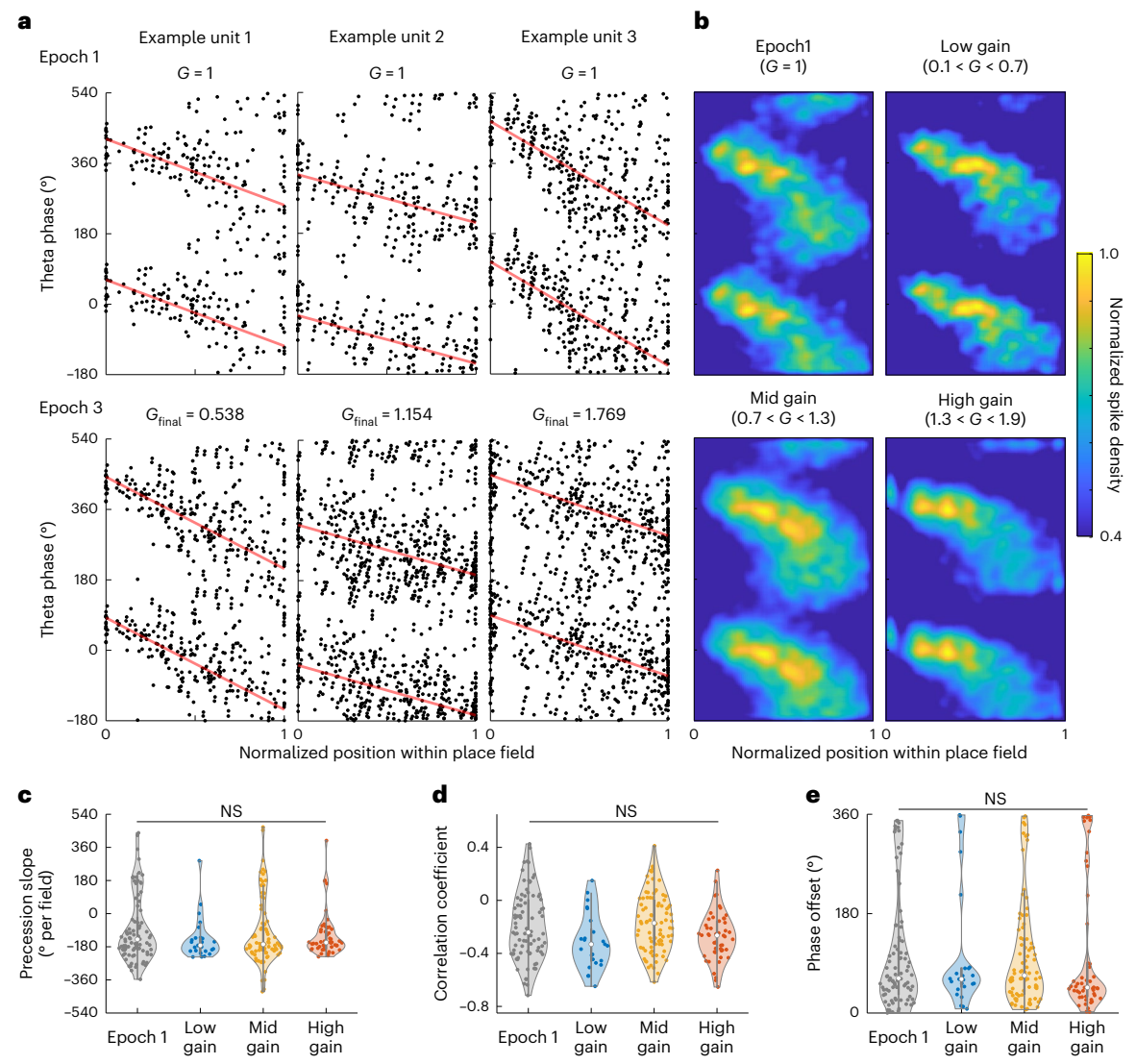


Fig. 2 | **Phase precession is maintained in the landmark frame of reference. a**, Position–phase plots of example units using normalized position. The x axis represents the normalized position within a place field, where the edges correspond to the start and the end of the place field. **b**, Smoothed position–phase plots using all spikes from all units for epoch 1(G=1), low gain (G=0.1-0.7), mid gain (G=0.7-1.3) and high gain (G=1.3-1.9) conditions. The x axis ranges from 0.01 to 0.99 to avoid the overconcentration of points at x=0 and x=1, because fields were defined as starting and ending at a spike. **c**, Precession slopes for each gain group (n=246 units). Overall: W(3)=1.08, P=0.781

(two-sided); Wald test on the LMEM. Each violin plot shows the median (white circle), interquartile range (gray line) and distribution outline. NS, not significant. ${\bf d}$, Circular–linear correlation coefficients for each gain group (n=246 units). Overall: W(3)=5.80, P=0.122 (two-sided); Wald test on the LMEM. ${\bf e}$, Phase offsets for each gain group (n=246 units). Epoch 1 versus low: P=0.769, epoch 1 versus mid: P=0.707, epoch 1 versus high: P=0.707, low versus mid: P=0.707, mid versus high: P=0.707; two-sided P values based on a hierarchical bootstrap test followed by FDR correction.

precession with gain, we hypothesized that the within-cycle sequential firing pattern would be preserved. To test this idea, we computed the pairwise coactivation pattern, a sensitive measure to quantify theta sequences that measures the theta-scale time lag between place cell pairs from the cross-correlogram (CCG) (Fig. 3e) 19 . The temporal offset of the CCG peak (or the theta-scale time lag) correlates with the distance between place cell pairs in a theta sequence, and the ratio of these two quantities (compression factor (CF)) can be used to measure the degree of sequence compression in a theta cycle. CF was invariant across gains (Fig. 3f), suggesting that the scaling of precession preserves the coherent theta sequence structure in the landmark frame.

Phase precession when allothetic cues are weak or absent

The analyses thus far have focused on conditions under which the hippocampal map was controlled by allothetic spatial cues. The findings can be interpreted in two ways. The first is that phase precession is a visually driven response directly controlled by the moving landmarks, akin to visually evoked firing in CA1 (ref. 61). The second is that the precession is controlled by the dynamics and circuitry of the internal hippocampal map, which happens to be locked to the external landmarks. To dissociate these two possibilities, we studied the temporal firing pattern of place cells in two different conditions: (1) when landmarks were turned off and (2) in 'landmark failure' sessions, in which the hippocampal map decoupled from the landmarks.

In condition (1), rats ran inside the Dome after landmarks were turned off after epoch 3 (that is, the start of epoch 4; Fig. 4a). Without salient landmarks, the place fields were not locked to the lab frame or any other external frame; rather, the spiking activity followed an internal hippocampal frame that was driven by idiothetic cues and strongly influenced by the previously experienced gain in epoch 3 (ref. 47) (Extended Data Fig. 3b). The gain of this frame, termed the hippocampal gain H, was computed from the spatial frequency spectrogram of

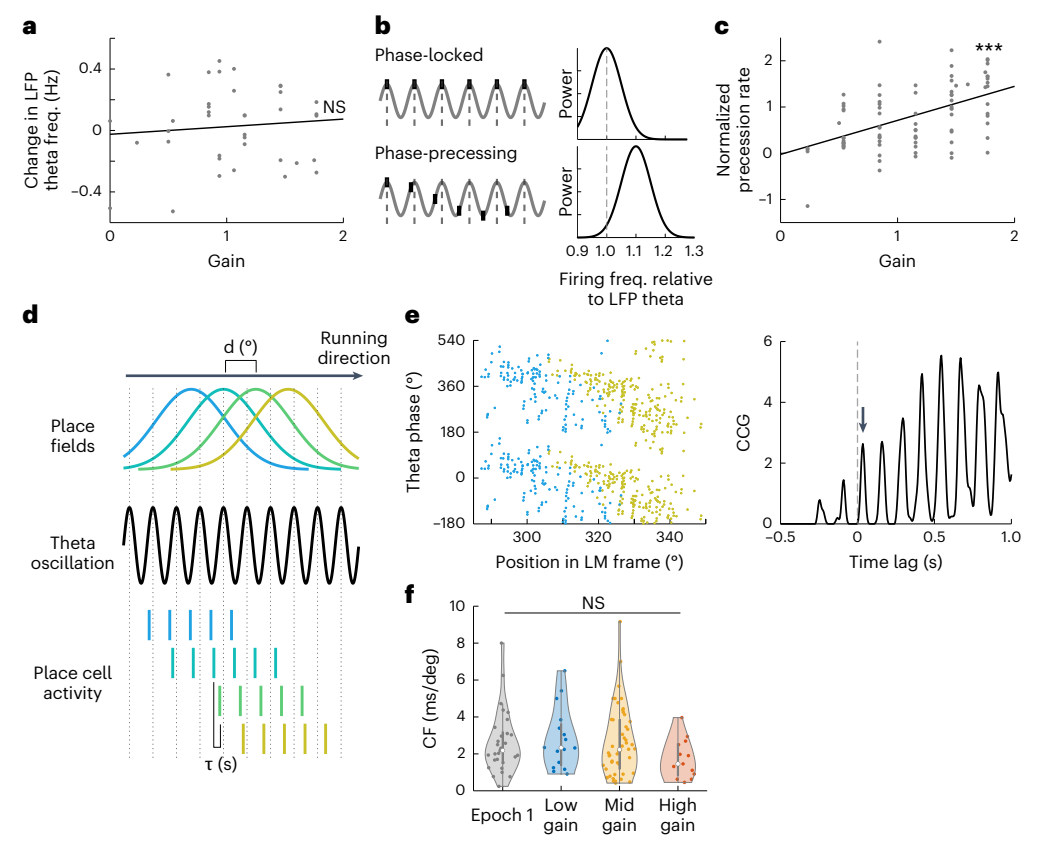


Fig. 3 | **Place cells scale their theta-modulated bursting frequency in response to the experimental gain. a**, Change in LFP theta frequency and experimental gain. Change in theta frequency is defined as the difference between the mean theta frequencies between epoch 3 and epoch 1. Dots indicate individual sessions, and the black line represents the best-fit line. Slope = 0.0495, $r^2 = 9.11 \times 10^{-3}$, $F_{1.36} = 0.331$, P = 0.569; F-test. **b**, Schematics of the spike phase spectrum analysis. Left: example theta-modulated bursting patterns. Sinusoidal curves represent the LFP theta oscillation, and black ticks represent bursts of spikes. Right: corresponding spike phase spectra. A spike phase spectrum with a peak at 1 would indicate that the spiking activity contains a component that is phase locked to the LFP theta (top). On the other hand, a peak at a value

greater than 1 would indicate a prominent precession (bottom). **c**, Normalized precession rates across gain values. Slope = 0.736, r^2 = 0.243, $F_{1,84}$ = 26.9, P = 1.45×10^{-6} ; F-test. **d**, Schematic of the formation of a theta sequence. Colored ticks represent bursting activities from respective place cells. **e**, Example place cell pair and its CCG. Left: position–phase plot of two place cells (blue, yellow) with overlapping fields. Right: CCG and its theta-scale time lag denoted by the arrow. The peaks appeared at a period matching the LFP theta (-125 ms). **f**, Compression factors for each gain group (n = 119 pairs). Overall: W(3) = 1.69, P = 0.640 (two-sided); Wald test on the LMEM. Each violin plot shows the median (white circle), interquartile range (gray line) and distribution outline. ***P < 0.001. LM, landmark; d, distance.

place cell firing (Extended Data Fig. 3a). Intuitively, H is the ratio of distance traveled in the internal, cognitive map divided by the distance traveled in the lab frame. Given that the constantly changing hippocampal gain during epoch 4 is incompatible with the NPR metric, we quantified phase precession using circular-linear regression (the same applies to condition (2)). In the landmarks-off condition, phase precession was locked to the hippocampal frame of reference (Fig. 4b). Other parameters were also invariant (Extended Data Fig. 3c,d). In condition (2), we looked at sessions in which the hippocampal gain (H) decoupled from one-to-one correspondence with the experimental gain (G) during epochs 2 and 3 (Fig. 4c). In these sessions, the map drifted as a coherent ensemble relative to both the experimentally controlled landmarks and the lab frame, demonstrating a weaker, or a lack of, control of the allothetic cues over the hippocampal map in these sessions (Extended Data Fig. 3e–g)^{62–64}. By limiting the analysis to laps with landmark failure (H/G less than 0.9 or greater than 1.1), we found that the precession was locked to the hippocampal frame of reference (Fig. 4d). Other parameters were also similar between the two groups except for a slight increase in the correlation coefficients in the landmark failure condition (Extended Data Fig. 3h,i). Overall, the results from conditions (1) and (2) demonstrate that the scaling of phase precession is a product of the hippocampal gain rather than a direct readout of allothetic inputs. Together with results from the

previous subsections, phase precession is a robust phenomenon that emerges in the frame of reference at which the spatial tuning of place cells is maintained.

Multiplexed theta phase coding revealed in single traversals

The results thus far demonstrated that phase precession is maintained in the hippocampal frame of reference under conditions of conflicting allothetic and idiothetic inputs. However, it is unclear whether phase 'procession' is also maintained under these conditions. To gain access to the detailed structure of phase coding, we analyzed the firing patterns of single traversals through the place fields. Single-traversal phase coding exhibited high lap-to-lap variability, in concordance with previous reports 41,65,66 (Fig. 5a). Interestingly, the overall distribution of single-traversal phase coding slopes was multimodal (Fig. 5b). Although the majority of traversals had negative slopes (mode = -160° per field), many traversals showed positive slopes (mode = 150° per field). Similarly, a large portion of single traversals exhibited positive correlation coefficients (Extended Data Fig. 4a,b). The observed positive slope could not be explained by a continuous precession combined with a sudden drop in firing rate around the center of the field (Extended Data Fig. 4c-f).

The prominence of positive position–phase correlation at the end of the field led us to hypothesize that the whole-field positive-slope

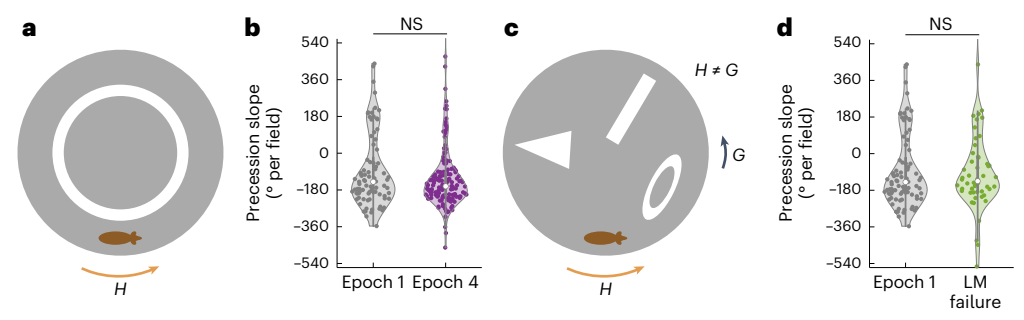


Fig. 4 | Phase precession is controlled by the hippocampal map when allothetic cues are weak or absent. a, Schematic of epoch 4. Only the spatially uninformative, overhead ring light was provided as a source of illumination. b, Precession slopes for epochs 1 and 4 (n = 233 units). $\beta = -18.9$, s.e. = 20.9, t(231) = -0.901, P = 0.368; t-statistics/two-sided P value from the LMEM. Each violin plot shows the median (white circle), interquartile range (gray line) and

distribution outline. **c**, Schematic of a landmark failure session. In these sessions, the place cells were locked to the hippocampal frame with a gain of H that differed from the experimental gain G. **d**, Precession slopes for epoch 1 and LM failure (n = 137 units). $\beta = 0.479$, s.e. = 33.3, t(135) = 0.0144, P = 0.989; t-statistics/ two-sided P value from the LMFM.

traversals may reflect traversals that contain bona fide phase processions in the second half of the field (as observed by Wang et al.³⁷), whereas whole-field negative-slope traversals reflect prominent precession throughout the field. Indeed, when we created position-phase plots using either only negative-slope or positive-slope traversals, we observed a clear difference in the theta phase occupancy (Fig. 5c). Although the negative-slope traversals resulted in a continuously precessing structure in the later phases of theta, positive-slope traversals exhibited a two-lobe structure, with components of initial phase precession at later phases and a second lobe at earlier phases of theta. The two-lobe structure became more evident when computing the difference between the two plots and thresholding at zero, which visualized the subspace in the position-phase space where one type of traversal contributed more than the other (Fig. 5d). The two lobes in Fig. 5d occur at theta phases where forward and reverse theta sequences have been observed³⁷ (forward window: -110° to 60°, reverse window: 80–230°), matching the association of phase precession and procession to forward and reverse theta sequences, respectively. By performing a circular-linear regression using spikes that belong to the forward or reverse windows³⁷, we confirmed that the two lobes indeed correspond to phase precession and procession (Fig. 5e.f). Similarly, spike phase spectrum analysis using only spikes from either one of the two windows showed lower NPRs in the reverse window compared with the forward window (Fig. 5g), indicating that the theta-modulated firing of place cells slowed down in the early phases of theta.

To quantify the difference in phase occupancy between the negative-slope and positive-slope traversals, we defined the second lobe index (SLI) as the proportion of total spikes that occurred in the reverse window. Positive-slope traversals showed a significantly higher contribution to the second lobe compared with the negative-slope traversals (Fig. 5h). The same qualitative effect was observed for all five individual animals (Fig. 5i; P = 0.0313; binomial test). Together, the prominence of procession within single traversals can be measured using both the slope of the circular–linear regression and SLIs.

Phase procession diminishes under cue conflict

Using single-traversal phase coding, we next asked how phase procession is affected under a persistent conflict between allothetic and idiothetic spatial cues, which requires continuous encoding of new relationships between the two cues 47,51 . By looking at the single-traversal slopes, we found that the proportion of positive-slope traversals decreased in low and high gains (that is, when G deviated from 1) (Fig. 6a). The effect was maintained even after limiting the analysis to traversals with strong firing (\geq 25 spikes), indicating that the observed difference is not due to traversals with weak firing that could yield

erroneous estimation of the slopes (Extended Data Fig. 4g). The correlation coefficient showed a similar effect (Extended Data Fig. 4h). The phase offset of single-traversal phase coding showed a complex response to gain, with a shift to earlier and later phases in low and mid gain conditions, respectively (Extended Data Fig. 4i). As predicted from the relationship between the sign of slopes and phase occupancy, the overall position-phase plots also demonstrated a diminished second lobe in the low and high gain conditions (Fig. 6b). In fact, whereas the mid gain condition showed SLIs similar to the G=1 condition, both low and high gain conditions exhibited decreased SLIs (Fig. 6c). The change in SLIs across gain conditions could not be explained by other variables, including theta frequency, traversal distance through the fields, animal's speed, time passage and sampling bias of unimodal/ bimodal cells (Extended Data Figs. 5 and 6). The results suggest that the constant encoding of new associations between allothetic and idiothetic inputs when $G \neq 1$, regardless of the sign of the error, selectively disrupts phase procession.

To further test the idea that phase procession requires a stable and coherent association of allothetic and idiothetic spatial inputs to the CA1 place cell network, we analyzed data from epoch 4, when visual landmarks were turned off. Given the absence of salient allothetic cues during epoch 4, the hippocampal map is driven primarily by idiothetic inputs. We observed that SLIs decreased in this condition compared with epoch 1, when salient allothetic cues were available (Fig. 6d and Extended Data Fig. 4j). The result is consistent with the increased demand to encode new associations between path integration inputs and less salient landmarks in the lab environment that were previously overshadowed by the prominent visual landmarks in the Dome.

Lastly, we asked how the incoherence in allothetic and idiothetic cues affected the two major input streams onto CA1:CA3 and entorhinal cortex layer III (ECIII). The strength of CA3 and medial ECIII inputs are thought to be reflected in the level of coupling of CA1 spikes with the slow and medium gamma oscillation in the LFP⁶⁷⁻⁷⁰ (Extended Data Fig. 7a; but see refs. 71,72). We quantified this interaction using spike-LFP coupling, which measures the degree of phase locking of spikes to different frequency components in the LFP. If allothetic and idiothetic inputs into CA1 are anatomically segregated into CA3 and ECIII pathways, we would expect that spike-LFP coupling to the input that provides allothetic information to be unaffected by the gain manipulation under landmark control, whereas the idiothetic input would be affected. Thus, the gain manipulation would affect only the low or medium gamma bands. On the other hand, if both CA3 and ECIII inputs conjunctively encode allothetic/idiothetic information, we would expect that spike-LFP coupling to both gamma bands to be altered. We observed that the spike-LFP coupling relative to the G = 1 condition was elevated during low and high gain manipulation in

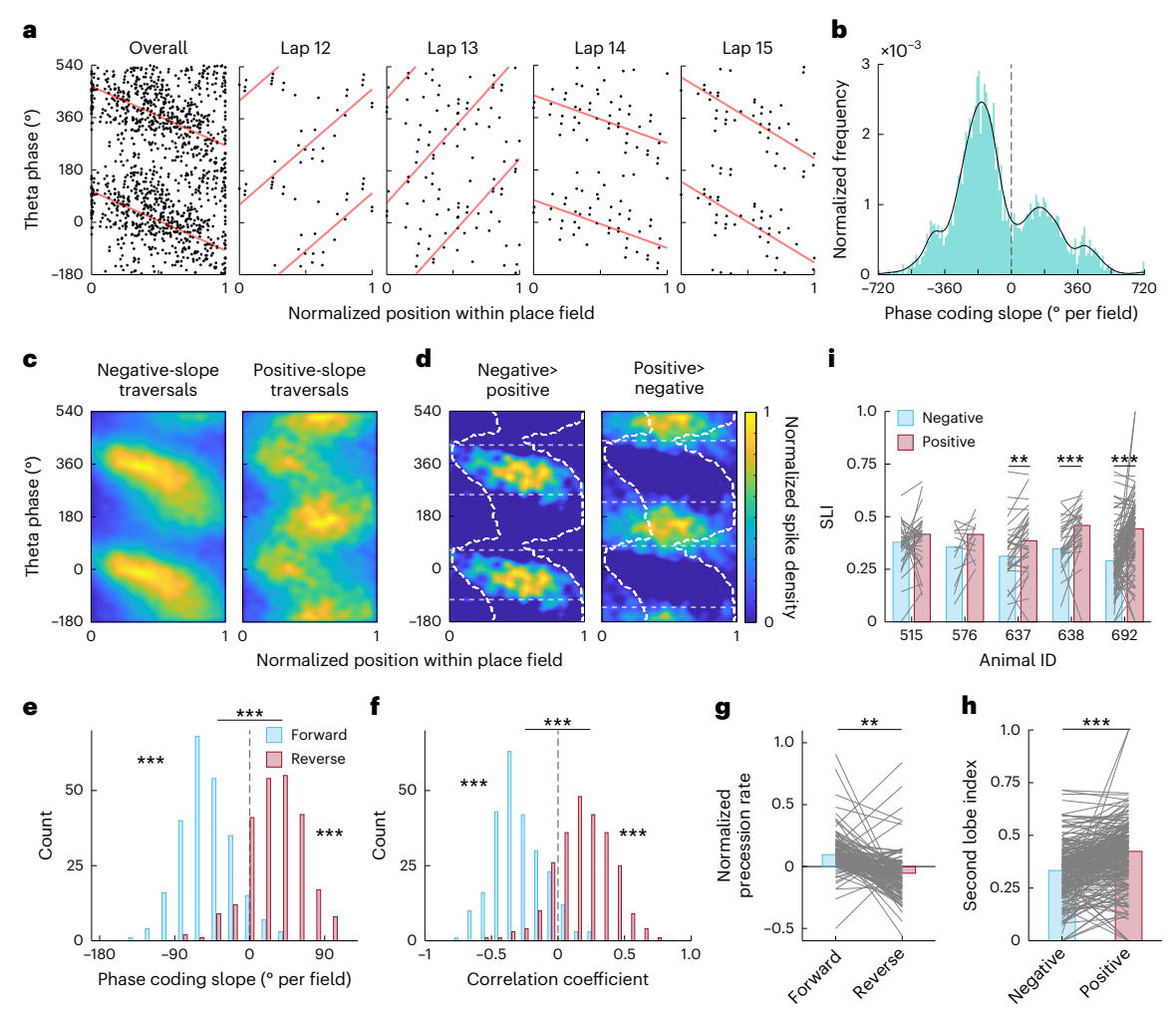


Fig. 5 | **Single-traversal analysis reveals the two-lobe structure of phase coding. a**, Overall (left) and single-traversal (right) phase coding of an example unit. Laps 12 and 13 show phase procession. **b**, Distribution of single-traversal slopes. **c**, Smoothed position–phase plots of negative-slope (left) and positive-slope (right) traversals. **d**, Difference in the two smoothed position–phase plots, with negative values set to 0. White dashed lines represent the contour of the overall phase coding structure. Gray horizontal dashed lines indicate the range of forward (-110° to 60° ; left) or reverse (80 to 230°; right) windows. **e**, Circular–linear regression slopes in the two windows. Forward: $\beta = -54.6$, s.e. = 3.76, t(490) = -14.5, $P = 1.03 \times 10^{-39}$; reverse: $\beta = 33.9$, s.e. = 3.76, t(490) = 9.02, $P = 4.23 \times 10^{-18}$; forward versus reverse: $\beta = 88.5$, s.e. = 5.32, t(490) = 16.6, $P = 4.35 \times 10^{-49}$; *t*-statistics/two-sided *P* values from the LMEM followed by FDR correction. **f**, Circular–linear correlation coefficients in the two windows. Forward: $\beta = -0.293$, s.e. = 0.0127, t(490) = -14.5, $P = 1.03 \times 10^{-39}$;

reverse: β = 0.184, s.e. = 0.0127, t(490) = 9.02, P = 4.23 × 10⁻¹⁸; forward versus reverse: β = 0.477, s.e. = 0.0180, t(490) = 16.6, P = 4.35 × 10⁻⁴⁹; t-statistics/ two-sided P values from the LMEM followed by FDR correction. \mathbf{g} , Normalized precession rates in the two windows (n = 148 pairs). β = -0.112, s.e. = 0.0406, t(294) = -2.76, P = 6.23 × 10⁻³; t-statistics/two-sided P value from the LMEM. \mathbf{h} , SLIs of negative-slope and positive-slope traversals (n = 226 pairs). β = 0.0856, s.e. = 9.86 × 10⁻³, t(450) = 8.68, P = 7.17 × 10⁻¹⁷; t-statistics/two-sided P value from the LMEM. \mathbf{i} , SLIs of negative-slope and positive-slope traversals for each animal (n = 226 pairs). Rat 515: β = 0.0287, s.e. = 0.0245, t(68) = 1.17, P = 0.246; rat 576: β = 0.0658, s.e. = 0.0388, t(24) = 1.70, P = 0.128; rat 637: β = 0.0662, s.e. = 0.0152, t(68) = 4.35, P = 1.19 × 10⁻⁴; rat 638: β = 0.0797, s.e. = 0.0187, t(60) = 4.25, P = 1.25 × 10⁻⁴; rat 692: β = 0.113, s.e. = 0.0158, t(222) = 7.17, P = 5.38 × 10⁻¹¹; t-statistics/two-sided P values from the LMEM followed by FDR correction. **P < 0.001, ***P < 0.001.

both the slow and the medium gamma range (Fig. 6e), although only the medium gain condition reached statistical significance (Fig. 6f,g and Extended Data Fig. 7b). The result demonstrates increased phase locking to medium, and potentially slow, gamma during gain manipulation, perhaps due to a decrease in more complex interactions between spiking and gamma oscillations, such as the gamma phase precession (that is, spiking activity advances in phase across slow gamma cycles) that would lower the phase locking in a control condition⁷³. The possibility that the interaction between spiking and both the CA3 and ECIII inputs are modulated by gain manipulation suggests that both inputs contain a conjunction of allothetic and idiothetic spatial information, with a potentially stronger influence of ECIII inputs when new associations between the two spatial cues are encoded (Supplementary Text 1).

A CAN model captures the modulation of the second lobe

To understand how increased demand to encode new associations between allothetic and idiothetic inputs may result in the diminishing of the second lobe, we used the CAN model of Chu et al. 38 that incorporates feedback inhibition to recapitulate both phase precession and procession (Fig. 7a). The feedback inhibition term V destabilizes the activity bump and allows it to oscillate around the external input, resulting in phase precession and procession. To dissociate the effect of allothetic and idiothetic inputs, we decomposed the unitary external input term in the original model into two Gaussian inputs, $I_{\rm allo}$ and $I_{\rm idio}$. The two Gaussians differ in amplitude such that the larger amplitude was assigned to the cue that had stronger control over the hippocampal map. For instance, during gain manipulation with landmark control, the allothetic bump was assigned a larger amplitude to match the

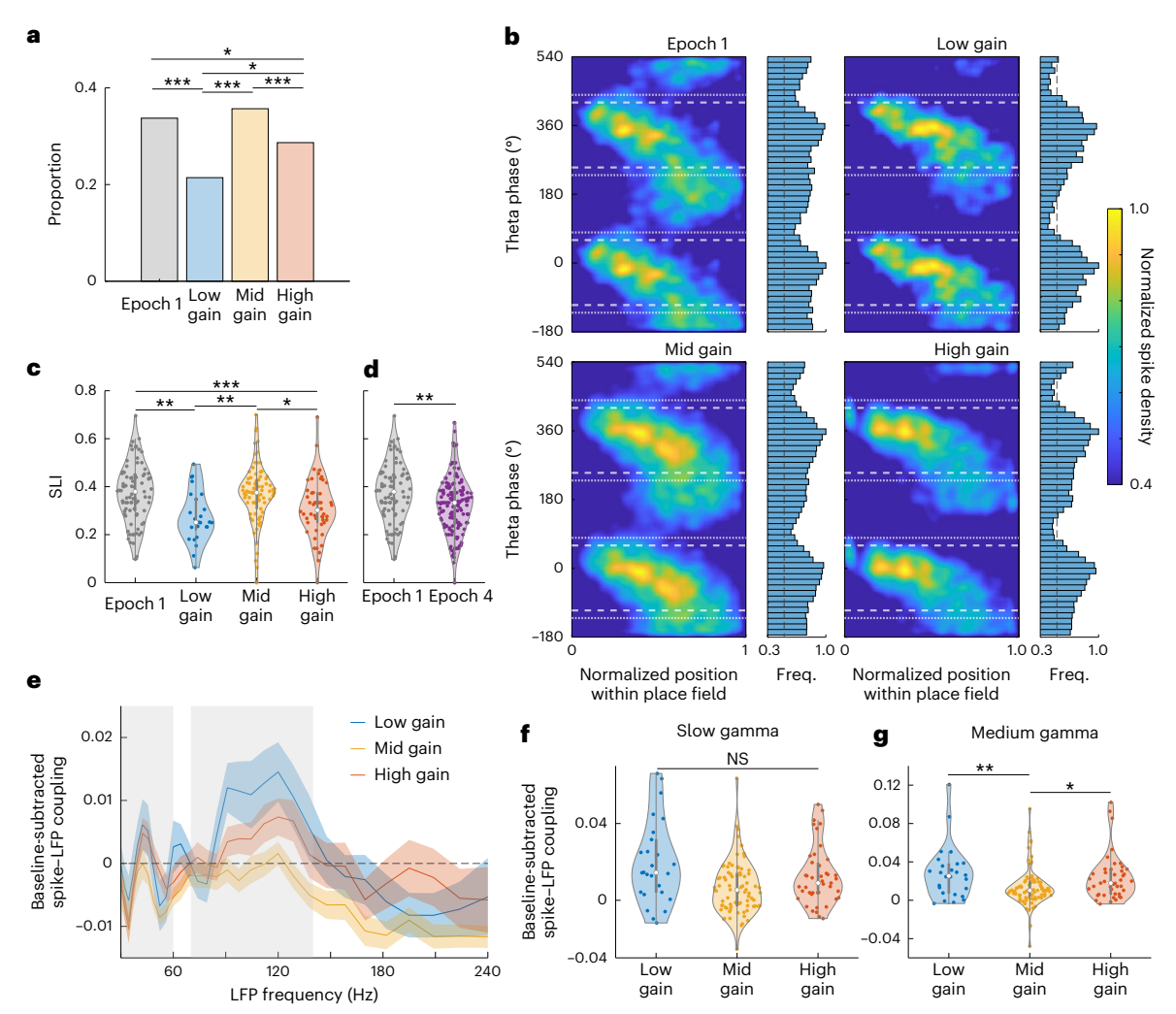


Fig. 6 | Phase procession is diminished under incoherent allothetic and idiothetic inputs. a, Proportion of positive single-traversal slopes. Overall: $\chi^2(3) = 36.24, P = 6.66 \times 10^{-8}; \text{ epoch 1 versus low: } \chi^2(1) = 14.07, P = 3.52 \times 10^{-4}, \text{ epoch 1 versus mid: } \chi^2(1) = 0.939, P = 0.333, \text{ epoch 1 versus high: } \chi^2(1) = 6.47, P = 0.0165, \text{ low versus mid: } \chi^2(1) = 21.28, P = 1.30 \times 10^{-5}, \text{ low versus high: } \chi^2(1) = 6.06, P = 0.0166, \text{ mid versus high: } \chi^2(1) = 21.11, P = 1.30 \times 10^{-5}; \text{ chi-squared test followed by FDR correction. } \mathbf{b}, \text{ Phase occupancy histograms. Dashed lines on the histogram indicate half maximum. Position-phase plots from Fig. 2c, with lines indicating the forward (dashed lines) and reverse (dotted lines) windows, are provided as a reference. <math>\mathbf{c}$, SLIs for each gain group (n = 246 units). Overall: $W(3) = 17.4, P = 5.89 \times 10^{-4}$ (two-sided); epoch 1 versus low: $\beta = 0.0920$, s.e. $= 0.0271, t(242) = 3.39, P = 8.10 \times 10^{-4}, \text{ epoch 1 versus mid: } \beta = 0.0133,$ s.e. $= 0.0184, t(242) = 0.724, P = 0.470, \text{ epoch 1 versus high: } \beta = 0.0638,$ s.e. $= 0.0213, t(242) = 3.00, P = 3.01 \times 10^{-3}, \text{ low versus mid: } \beta = -0.078, \text{ s.e.} = 0.0277, <math>t(242) = -2.84, P = 4.85 \times 10^{-3}, \text{ low versus high: } \beta = -0.0282, \text{ s.e.} = 0.0293,$

t(242) = -0.961, P = 0.337, mid versus high: $\beta = 0.0505$, s.e. = 0.0216, t(242) = 2.34, P = 0.0200; Wald test followed by t-statistics/two-sided P values from the LMEM. Each violin plot shows the median (white circle), interquartile range (gray line) and distribution outline. \mathbf{d} , SLIs in epochs 1 and 4 (n = 233 units). $\beta = -0.0419$, s.e. $= 0.0159, t(231) = -2.63, P = 9.05 \times 10^{-3}; t$ -statistics/two-sided P value from the LMEM. \mathbf{e} , Spike-LFP coupling relative to baseline (epoch 1). Each line shows mean \pm s.e. The gray-shaded regions correspond to frequency ranges of slow and medium gamma. \mathbf{f} , Spike-slow gamma coupling (n = 151 units). Overall: W(2) = 2.21, P = 0.331 (two-sided); Wald test from the LMEM. \mathbf{g} , Spike-medium gamma coupling (n = 151 units). Overall: $W(2) = 11.7, P = 2.89 \times 10^{-3}$ (two-sided); low versus mid: $\beta = 0.0148$, s.e. $= 4.96 \times 10^{-3}, t(148) = 2.99, P = 3.29 \times 10^{-3}$, low versus high: $\beta = 4.64 \times 10^{-3}$, s.e. $= 5.48 \times 10^{-3}, t(148) = 0.848, P = 0.398$, mid versus high: $\beta = -0.0102$, s.e. $= 4.15 \times 10^{-3}, t(148) = -2.45, P = 0.0154$; Wald test followed by t-statistics/two-sided P values from the LMEM. *P < 0.05, **P < 0.01, ***P < 0.001.

observation that the overall place cell map was stable in the landmark frame. Note that when G=1, the two Gaussians add up to a single Gaussian, and thus the dynamics were equivalent to the original model. When the two bumps were misaligned (that is, gain manipulation), the idiothetic bump was periodically aligned to the allothetic bump to account for the effect of allothetic cues correcting accumulated path integration error $^{74-76}$.

Using this modified CAN model, we tested how gain manipulation affects phase coding. Under landmark control, the place cells are locked to the allothetic inputs. As the gain deviates from 1 in either direction, the corresponding idiothetic inputs will lag (G > 1) or lead (G < 1) the activity bump in the cognitive map that is excited by the allothetic cues. In other words, the place cell that is activated at a given moment

will receive reduced excitation due to the decreased contribution of the idiothetic-driven position inputs onto that cell, as the idiothetic bump excites neurons on either side of the allothetic bump (Fig. 7b). Note that the activity bump moves in the same direction as the external input during phase precession; in contrast, the activity bump moves in the opposite direction as the external input during procession. Due to this asymmetry in direction, which makes phase procession more sensitive to the strength of feedback inhibition compared with phase precession 38 , the decreased excitation (hence the relative increase in feedback inhibition strength) should selectively impair phase procession. Under the G = 1 condition, when the place cell network is excited by a unitary Gaussian input, the model units exhibit both phase precession and procession (Fig. 7c, middle, and Supplementary Table 3). When

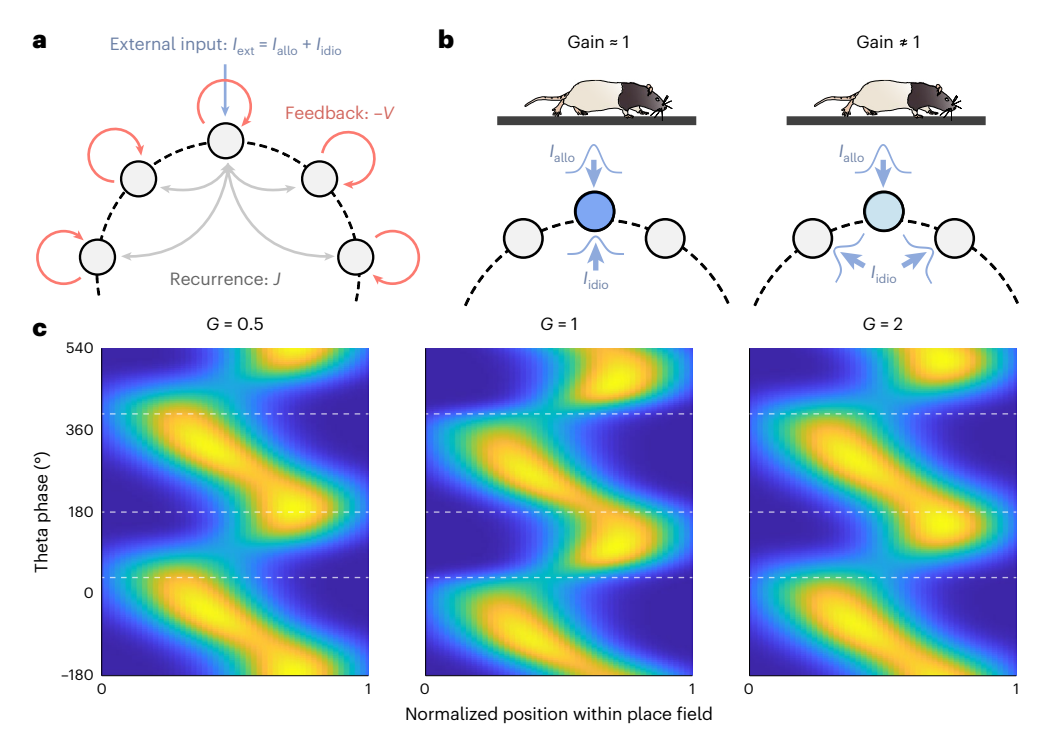


Fig. 7 | **CAN model explains the selective diminishment of phase procession. a**, Schematic of the CAN model. The nodes represent individual place fields that are arranged as a ring attractor to match the topology of the circular track. Each node receives an excitatory input I, a recurrent excitatory input J and feedback inhibition components V. **b**, Conceptual schematics of the effect of gain. When the experimental gain is close to 1, allothetic and idiothetic inputs provide

coherent excitation to the place cell network, as the two inputs become coupled during the prior experience. As gain deviates from 1, the incoherence in the two inputs results in a reduced excitation of the activity bump, indicated by the lighter shading of the active neuron. \mathbf{c} , Position–phase plots of model neurons experiencing different experimental gains. Image of rat in \mathbf{b} adapted from SciDraw 93 .

the allothetic input moves faster (G=2) or slower (G=0.5) than the idiothetic input, we confirm our prediction of a decrease in the size of the processing lobe with minimal effect on the precessing lobe (Fig. 7c, left/right). Similarly, the processing lobe diminished when the allothetic input was ablated, mimicking epoch 4 where subtle local cues are not yet established as landmarks (Extended Data Fig. 7c, d). Thus, the CAN model provides a mechanistic explanation of how novel associations of allothetic and idiothetic inputs selectively diminish phase procession at the early phases of theta (Supplementary Text 2).

Discussion

Previous studies on the theta phase coding by CA1 place cells largely focused on phase precession. Using a virtual reality system that promotes the continuous encoding of new associations between allothetic and idiothetic inputs, we show that the early and late phases of theta contain functionally distinct phase codes. Although phase precession remained intact in the internal hippocampal frame during the encoding of spatial inputs, the prominence of phase procession was impaired. This asymmetric response was captured using a CAN model. The results demonstrate that theta phase coding consists of two modes that differ in their reliance on spatial cues and how they may support distinct computational processes within a theta cycle.

The locking of phase precession to the hippocampal frame of reference emphasizes the adaptability of the temporal firing pattern of the place cells. The scaling of phase precession was observed previously in conditions where a familiar linear track was shortened ^{14,55} (see also refs. 54,56 for stretching of place fields with weakened self-motion inputs). We extend these findings and show that the scaling can happen even when the hippocampal map dissociates from external landmarks, indicating that the scaling cannot be solely explained by the change in the perceptual speed derived from a specific, allothetic input; rather, the precession speed relative to the field size is invariant

in the hippocampal map. Such scaling might be synchronized among the place cells by the intrinsic network connectivity ^{42,77}, as shown by the preservation of theta-related co-firing patterns between place cell pairs. Furthermore, studies using various ramping gain profiles in epoch 2 will allow us to test whether scaling in theta-modulated firing frequencies occurs continuously or in discrete steps, perhaps quantized by the theta-nested gamma oscillations²⁹.

In contrast to phase precession, theta-modulated activity at the earlier phases of theta is much less understood. Our study extends the current understanding of this two-lobe structure of phase coding in two important ways. First, we describe a connection between the two lobes and trial-by-trial variability. Although phase coding has been shown to exhibit variability on single traversals, sometimes exhibiting positive slopes⁶⁵, the observation remained largely unexplained. Our study shows that negative-slope (that is, net precession) and positive-slope (that is, net procession) traversals consist of spikes with different theta phase preferences, such that they mainly contribute to the major and the minor lobes of phase coding, respectively. Furthermore, this relationship may relate to another line of studies demonstrating that different types of gamma oscillations that are coupled to the ongoing theta oscillation affect place cell firing 73,78,79. Because the precessing and the processing lobes occupy theta phase ranges that match the preference of slow and medium gamma oscillations, the variability in single-traversal phase coding, two-lobe structures and different thetagamma coupling states may be all the same phenomena described through different lenses.

Second, procession was impaired as the experimental gain deviated bidirectionally from 1, where the large conflict between the spatial cues forced the system to encode a new mapping of allothetic cues onto the idiothetic cue-driven internal map every lap. This finding suggests that the two modes of phase coding are not only different in terms of the theta-modulated spiking activity that makes them

up (precession versus procession) but also in terms of the types of spatial cues that contribute to them; whereas phase precession is controlled by the most prominent cue (idiothetic or allothetic) in a seemingly winner-take-all manner, phase procession may require a more balanced level of excitation from these cues. One speculation is that the variability in single-traversal phase coding during the G=1condition reflects the degree of drift between the allothetic and idiothetic maps, potentially caused by the amount of attention paid to external landmarks. This view matches the result of a different study where error trials during a delayed match-to-place task biased the place cell firing to later phases of theta, likely due to the discrepancy between internal estimates of the location and the actual position²⁵. Interestingly, another study also reported a shift in theta phase preference inside a body-fixed virtual reality setup that causes conflict within self-motion cues⁸⁰, which may reflect a similar phenomenon observed here.

What does the dissociation of the two modes of phase coding tell us about their functional roles? The two ranges of theta have been implicated in distinct functional properties. In the late phases of theta, place cells exhibit phase precession that leads to the prediction of future trajectories via forward theta sequences^{22-25,81,82}. In the early phases of theta, two processes are hypothesized to take place. First, in the framework proposed by Hasselmo et al. ^{9,31}, the early theta phase range is specific for the encoding of new information, where the level of plasticity is heightened^{32,33}. By allowing dendritic depolarization to induce plasticity at individual synapses while suppressing axonal spiking activity, the network can reduce interference between the new association and previously stored associations (memories) that might be activated by the current inputs. Such subthreshold plasticity in hippocampal cells was shown ex vivo³⁴ and was later observed in place cells in vivo³⁶. Second, the spiking activity in the early phases of theta as rats navigated a familiar environment, where the cognitive map is already established, formed a retrospective (reverse) theta sequence; such reverse-ordered sequences are hypothesized to serve as the substrate of reverse replay events for value learning during subsequent rest epochs^{37,83}. These ideas can be unified into a framework where late phases of theta are reserved for phase precession-based prediction, whereas early phases of theta can be used for either encoding or phase procession-based reversed retrospective sequences, depending on the cognitive demand.

The framework described above concurs with the results of the present study. Our discovery of a substantial loss of spiking in the early theta phase when there is an error between the path integration prediction of location and the landmark-based location information strongly supports the model of Hasselmo et al. 9,31, as this spatial prediction error is likely to be the signal that generates plasticity to recalibrate the path integration gain^{47,50,51}. At the same time, the reduced occurrence of phase procession and reverse theta sequences will likely reduce the reverse replay-based consolidation of these states, where the association of allothetic and idiothetic cues is not established. Notably, such switching in the firing pattern spares the activity at later phases of theta and preserves the ability to continuously predict the animal's future location. Given that theta phase coding is also observed during non-spatial behaviors 77,84-88 and in numerous brain regions⁸⁹⁻⁹², the different dynamics of phase precession and procession may serve as a general circuit logic that allows flexible control of prospective representation, retrospective evaluation and encoding of new information.

Online content

Any methods, additional references, Nature Portfolio reporting summaries, source data, extended data, supplementary information, acknowledgements, peer review information; details of author contributions and competing interests; and statements of data and code availability are available at https://doi.org/10.1038/s41593-025-02038-6.

References

- Tolman, E. C. Cognitive maps in rats and men. Psychol. Rev. 55, 189–208 (1948).
- Tulving, E. & Donaldson, W. Organization of Memory (Academic Press. 1972).
- 3. O'Keefe, J. & Dostrovsky, J. The hippocampus as a spatial map: preliminary evidence from unit activity in the freely-moving rat. *Brain Res.* **34**, 171–175 (1971).
- 4. O'Keefe, J. Place units in the hippocampus of the freely moving rat. *Exp. Neurol.* **51**, 78–109 (1976).
- O'Keefe, J. & Nadel, L. The Hippocampus as a Cognitive Map (Oxford Univ. Press. 1978).
- Robinson, N. T. M. et al. Targeted activation of hippocampal place cells drives memory-guided spatial behavior. Cell 183, 1586–1599 (2020).
- Vanderwolf, C. H. Hippocampal electrical activity and voluntary movement in the rat. Electroencephalogr. Clin. Neurophysiol. 26, 407–418 (1969).
- Buzsáki, G. Theta oscillations in the hippocampus. Neuron 33, 325–340 (2002).
- Hasselmo, M. E. What is the function of hippocampal theta rhythm?—Linking behavioral data to phasic properties of field potential and unit recording data. *Hippocampus* 15, 936–949 (2005).
- O'Keefe, J. & Recce, M. L. Phase relationship between hippocampal place units and the EEG theta rhythm. *Hippocampus* 3, 317–330 (1993).
- Skaggs, W. E., McNaughton, B. L., Wilson, M. A. & Barnes, C. A. Theta phase precession in hippocampal neuronal populations and the compression of temporal sequences. *Hippocampus* 6, 149–172 (1996).
- 12. Jensen, O. & Lisman, J. E. Position reconstruction from an ensemble of hippocampal place cells: contribution of theta phase coding. *J. Neurophysiol.* **83**, 2602–2609 (2000).
- Mehta, M. R., Lee, A. K. & Wilson, M. A. Role of experience and oscillations in transforming a rate code into a temporal code. *Nature* 417, 741–746 (2002).
- Huxter, J., Burgess, N. & O'Keefe, J. Independent rate and temporal coding in hippocampal pyramidal cells. Nature 425, 828–832 (2003).
- O'Keefe, J. & Burgess, N. Dual phase and rate coding in hippocampal place cells: theoretical significance and relationship to entorhinal grid cells. *Hippocampus* 15, 853–866 (2005).
- Geisler, C., Robbe, D., Zugaro, M., Sirota, A. & Buzsáki, G. Hippocampal place cell assemblies are speed-controlled oscillators. Proc. Natl Acad. Sci. USA 104, 8149–8154 (2007).
- Huxter, J. R., Senior, T. J., Allen, K. & Csicsvari, J. Theta phasespecific codes for two-dimensional position, trajectory and heading in the hippocampus. *Nat. Neurosci.* 11, 587–594 (2008).
- Harvey, C. D., Collman, F., Dombeck, D. A., & Tank, D. W. Intracellular dynamics of hippocampal place cells during virtual navigation. *Nature* 461, 941–946 (2009).
- Dragoi, G. & Buzsáki, G. Temporal encoding of place sequences by hippocampal cell assemblies. Neuron 50, 145–157 (2006).
- 20. Foster, D. J. & Wilson, M. A. Hippocampal theta sequences. Hippocampus 17, 1093–1099 (2007).
- Foster, D. J. & Knierim, J. J. Sequence learning and the role of the hippocampus in rodent navigation. *Curr. Opin. Neurobiol.* 22, 294–300 (2012).
- 22. Johnson, A. & Redish, A. D. Neural ensembles in CA3 transiently encode paths forward of the animal at a decision point. *J. Neurosci.* 27, 12176–12189 (2007).
- Wikenheiser, A. M. & Redish, A. D. Hippocampal theta sequences reflect current goals. *Nat. Neurosci.* 18, 289–294 (2005).

- Kay, K. et al. Constant sub-second cycling between representations of possible futures in the hippocampus. Cell 180, 552–567 (2020).
- Zheng, C., Hwaun, E., Loza, C. A. & Colgin, L. L. Hippocampal place cell sequences differ during correct and error trials in a spatial memory task. *Nat. Commun.* 12, 3373 (2021).
- 26. Eliav, T. et al. Nonoscillatory phase coding and synchronization in the bat hippocampal formation. *Cell* **175**, 1119–1130 (2018).
- Qasim, S. E., Fried, I. & Jacobs, J. Phase precession in the human hippocampus and entorhinal cortex. Cell 184, 3242–3255 (2021).
- Hopfield, J. J. Pattern recognition computation using action potential timing for stimulus representation. *Nature* 376, 33–36 (1995).
- Lisman, J. The theta/gamma discrete phase code occuring during the hippocampal phase precession may be a more general brain coding scheme. *Hippocampus* 15, 913–922 (2005).
- Yamaguchi, Y., Aota, Y., McNaughton, B. L. & Lipa, P. Bimodality of theta phase precession in hippocampal place cells in freely running rats. J. Neurophysiol. 87, 2629–2642 (2002).
- Hasselmo, M. E., Bodelón, C. & Wyble, B. P. A proposed function for hippocampal theta rhythm: separate phases of encoding and retrieval enhance reversal of prior learning. *Neural Comput.* 14, 793–817 (2002).
- Huerta, P. T. & Lisman, J. E. Heightened synaptic plasticity of hippocampal CA1 neurons during a cholinergically induced rhythmic state. *Nature* 364, 723–725 (1993).
- Hölscher, C., Anwyl, R. & Rowan, M. J. Stimulation on the positive phase of hippocampal theta rhythm induces long-term potentiation that can be depotentiated by stimulation on the negative phase in area CA1 in vivo. J. Neurosci. 17, 6470–6477 (1997).
- Golding, N. L., Staff, N. P. & Spruston, N. Dendritic spikes as a mechanism for cooperative long-term potentiation. *Nature* 418, 326–331 (2002).
- Sheffield, M. E. J. & Dombeck, D. A. Calcium transient prevalence across the dendritic arbour predicts place field properties. *Nature* 517, 200–204 (2015).
- Sheffield, M. E. J., Adoff, M. D. & Dombeck, D. A. Increased prevalence of calcium transients across the dendritic arbor during place field formation. *Neuron* 96, 490–504 (2017).
- Wang, M., Foster, D. J. & Pfeiffer, B. E. Alternating sequences of future and past behavior encoded within hippocampal theta oscillations. Science 370, 247–250 (2020).
- Chu, T. et al. Firing rate adaptation affords place cell theta sweeps, phase precession and procession. eLife 12, RP87055 (2024).
- McNaughton, B. L. et al. Deciphering the hippocampal polyglot: the hippocampus as a path integration system. *J. Exp. Biol.* 199, 173–185 (1996).
- Chen, G., King, J. A., Burgess, N. & O'Keefe, J. How vision and movement combine in the hippocampal place code. *Proc. Natl Acad. Sci. USA* 110, 378–383 (2013).
- Cabral, H. O. et al. Oscillatory dynamics and place field maps reflect hippocampal ensemble processing of sequence and place memory under NMDA receptor control. *Neuron* 81, 402–415 (2014).
- Wang, Y., Romani, S., Lustig, B., Leonardo, A. & Pastalkova, E. Theta sequences are essential for internally generated hippocampal firing fields. *Nat. Neurosci.* 18, 282–288 (2015).
- Fattahi, M., Sharif, F., Geiller, T. & Royer, S. Differential representation of landmark and self-motion information along the CA1 radial axis: self-motion generated place fields shift toward landmarks during septal inactivation. *J. Neurosci.* 38, 6766–6778 (2018).
- O'Keefe, J. & Conway, D. H. Hippocampal place units in the freely moving rat: why they fire where they fire. *Exp. Brain Res.* 31, 573–590 (1978).

- Muller, R. U. & Kubie, J. L. The effects of changes in the environment on the spatial firing of hippocampal complex-spike cells. J. Neurosci. 7, 1951–1968 (1987).
- Acharya, L., Aghajan, Z. M., Vuong, C., Moore, J. J. & Mehta, M. R. Causal influence of visual cues on hippocampal directional selectivity. Cell 164, 197–207 (2016).
- Jayakumar, R. P. et al. Recalibration of path integration in hippocampal place cells. *Nature* 566, 533–537 (2019).
- 48. Mittelstaedt, M.-L. & Mittelstaedt, H. Homing by path integration in a mammal. *Naturwissenschaften* **67**, 566–567 (1980).
- 49. Etienne, A. S. & Jeffery, K. J. Path integration in mammals. Hippocampus 14, 180–192 (2004).
- Madhav, M. S. et al. The Dome: a virtual reality apparatus for freely locomoting rodents. J. Neurosci. Methods 368, 109336 (2022).
- Secer, G., Knierim, J. J. & Cowan, N. J. Continuous bump attractor networks require explicit error coding for gain recalibration. Preprint at *bioRxiv* https://doi.org/10.1101/2024.02.12.579874 (2024).
- Maurer, A. P., Cowen, S. L., Burke, S. N., Barnes, C. A. & McNaughton, B. L. Organization of hippocampal cell assemblies based on theta phase precession. *Hippocampus* 16, 785–794 (2006).
- 53. Kempter, R., Leibold, C., Buzsáki, G., Diba, K. & Schmidt, R. Quantifying circular-linear associations: hippocampal phase precession. *J. Neurosci. Methods* **207**, 113–124 (2012).
- 54. Terrazas, A. et al. Self-motion and the hippocampal spatial metric. *J. Neurosci.* **25**, 8085–8096 (2005).
- 55. Diba, K. & Buzsáki, G. Hippocampal network dynamics constrain the time lag between pyramidal cells across modified environments. *J. Neurosci.* **28**, 13448–13456 (2008).
- Ormond, J. & McNaughton, B. L. Place field expansion after focal MEC inactivations is consistent with loss of Fourier components and path integrator gain reduction. *Proc. Natl Acad. Sci. USA* 112, 4116–4121 (2015).
- Mizuseki, K., Sirota, A., Pastalkova, E. & Buzsáki, G. Theta oscillations provide temporal windows for local circuit computation in the entorhinal-hippocampal loop. *Neuron* 64, 267–280 (2009).
- King, C., Recce, M. & O'Keefe, J. The rhythmicity of cells of the medial septum/diagonal band of Broca in the awake freely moving rat: relationships with behaviour and hippocampal theta. *Eur. J. Neurosci.* 10, 464–477 (1998).
- Deshmukh, S. S., Yoganarasimha, D., Voicu, H. & Knierim, J. J. Theta modulation in the medial and the lateral entorhinal cortices. J. Neurophysiol. 104, 994–1006 (2010).
- Brandon, M. P., Bogaard, A. R., Schultheiss, N. W. & Hasselmo, M. E. Segregation of cortical head direction cell assemblies on alternating theta cycles. *Nat. Neurosci.* 16, 739–748 (2013).
- Purandare, C. S. et al. Moving bar of light evokes vectorial spatial selectivity in the immobile rat hippocampus. *Nature* 602, 461–467 (2022).
- 62. Knierim, J. J., Kudrimoti, H. S. & McNaughton, B. L. Place cells, head direction cells, and the learning of landmark stability. *J. Neurosci.* **15**, 1648–1659 (1995).
- 63. Rotenberg, A. & Muller, R. U. Variable place–cell coupling to a continuously viewed stimulus: evidence that the hippocampus is part of a perceptual system. *Philos. Trans. R. Soc. Lond. Ser. B* **352**, 1505–1513 (1997).
- Knierim, J. J., Kudrimoti, H. S. & McNaughton, B. L. Interactions between idiothetic cues and external landmarks in the control of place cells and head direction cells. J. Neurophysiol. 80, 425–446 (1998).
- Schmidt, R. et al. Single-trial phase precession in the hippocampus. J. Neurosci. 29, 13232–13241 (2009).

- Feng, T., Silva, D. & Foster, D. J. Dissociation between the experience-dependent development of hippocampal theta sequences and single-trial phase precession. *J. Neurosci.* 35, 4890–4902 (2015).
- Colgin, L. L. et al. Frequency of gamma oscillations routes flow of information in the hippocampus. *Nature* 462, 353–357 (2009).
- Schomburg, E. W. et al. Theta phase segregation of input-specific gamma patterns in entorhinal-hippocampal networks. *Neuron* 84, 470–485 (2014).
- Fernández-Ruiz, A. et al. Entorhinal–CA3 dual-input control of spike timing in the hippocampus by theta-gamma coupling. Neuron 93, 1213–1226 (2017).
- Palmigiano, A., Geisel, T., Wolf, F. & Battaglia, D. Flexible information routing by transient synchrony. *Nat. Neurosci.* 20, 1014–1022 (2017).
- 71. Zhou, Y. et al. Theta dominates cross-frequency coupling in hippocampal-medial entorhinal circuit during awake-behavior in rats. *iScience* **25**, 105457 (2022).
- Douchamps, V., di Volo, M., Torcini, A., Battaglia, D. & Goutagny, R. Gamma oscillatory complexity conveys behavioral information in hippocampal networks. Nat. Commun. 15, 1849 (2024).
- Zheng, C., Bieri, K. W., Hsiao, Y.-T. & Colgin, L. L. Spatial sequence coding differs during slow and fast gamma rhythms in the hippocampus. *Neuron* 89, 398–408 (2016).
- McNaughton, B. L., Chen, L. L. & Markus, E. J. 'Dead reckoning,' landmark learning, and the sense of direction: a neurophysiological and computational hypothesis. J. Cogn. Neurosci. 3, 190–202 (1991).
- Redish, A. D. & Touretzky, D. S. Cognitive maps beyond the hippocampus. *Hippocampus* 7, 15–35 (1997).
- Hardcastle, K., Ganguli, S. & Giocomo, L. M. Environmental boundaries as an error correction mechanism for grid cells. *Neuron* 86, 827–839 (2015).
- Pastalkova, E., Itskov, V., Amarasingham, A. & Buzsáki, G. Internally generated cell assembly sequences in the rat hippocampus. Science 321, 1322–1327 (2008).
- Bieri, K. W., Bobbitt, K. N. & Colgin, L. L. Slow and fast γ rhythms coordinate different spatial coding modes in hippocampal place cells. Neuron 82, 670–681 (2014).
- Guardamagna, M., Stella, F. & Battaglia, F. P. Heterogeneity of network and coding states in mouse CA1 place cells. *Cell Rep.* 42, 112022 (2023).
- 80. Aghajan, Z. M. et al. Impaired spatial selectivity and intact phase precession in two-dimensional virtual reality. *Nat. Neurosci.* **18**, 121–128 (2015).
- Gupta, A. S., van der Meer, M. A. A., Touretzky, D. S. & Redish, A. D. Segmentation of spatial experience by hippocampal theta sequences. *Nat. Neurosci.* 15, 1032–1039 (2012).

- 82. Maurer, A. P., Burke, S. N., Lipa, P., Skaggs, W. E. & Barnes, C. A. Greater running speeds result in altered hippocampal phase sequence dynamics. *Hippocampus* **22**, 737–747 (2012).
- 83. Ambrose, R. E., Pfeiffer, B. E. & Foster, D. J. Reverse replay of hippocampal place cells is uniquely modulated by changing reward. *Neuron* **91**, 1124–1136 (2016).
- Harris, K. D. et al. Spike train dynamics predicts theta-related phase precession in hippocampal pyramidal cells. *Nature* 417, 738–741 (2022).
- 85. Takahashi, M., Nishida, H., David Redish, A. & Lauwereyns, J. Theta phase shift in spike timing and modulation of gamma oscillation: a dynamic code for spatial alternation during fixation in rat hippocampal area CA1. *J. Neurophysiol.* 111, 1601–1614 (2014).
- Robinson, N. T. M. et al. Medial entorhinal cortex selectively supports temporal coding by hippocampal neurons. *Neuron* 94, 677–688 (2017).
- 87. Terada, S., Sakurai, Y., Nakahara, H. & Fujisawa, S. Temporal and rate coding for discrete event sequences in the hippocampus. *Neuron* **94**, 1248–1262 (2017).
- 88. Shimbo, A., Izawa, E.-l. & Fujisawa, S. Scalable representation of time in the hippocampus. *Sci. Adv.* **7**, eabd7013 (2021).
- 89. Jones, M. W. & Wilson, M. A. Phase precession of medial prefrontal cortical activity relative to the hippocampal theta rhythm. *Hippocampus* **15**, 867–873 (2005).
- 90. Hafting, T., Fyhn, M., Bonnevie, T., Moser, M.-B. & Moser, E. I. Hippocampus-independent phase precession in entorhinal grid cells. *Nature* **453**, 1248–1252 (2008).
- 91. van der Meer, M. A. A. & Redish, A. D. Theta phase precession in rat ventral striatum links place and reward information. J. Neurosci. **31**, 2843–2854 (2011).
- 92. Kim, S. M., Ganguli, S. & Frank, L. M. Spatial information outflow from the hippocampal circuit: distributed spatial coding and phase precession in the subiculum. *J. Neurosci.* **32**, 11539–11558 (2012).
- 93. Asiminas, A. Adult_Hooded_Rat_Running. Zenodo https://doi.org/10.5281/zenodo.3926277 (2020).

Publisher's note Springer Nature remains neutral with regard to jurisdictional claims in published maps and institutional affiliations.

Springer Nature or its licensor (e.g. a society or other partner) holds exclusive rights to this article under a publishing agreement with the author(s) or other rightsholder(s); author self-archiving of the accepted manuscript version of this article is solely governed by the terms of such publishing agreement and applicable law.

© The Author(s), under exclusive licence to Springer Nature America, Inc. 2025

Methods

All animal care, housing procedures and experimental procedures complied with National Institutes of Health guidelines and followed protocols approved by the Institutional Animal Care and Use Committee at Johns Hopkins University.

Subjects

Five male Long–Evans rats (Envigo Harlan; 5-8 months old at the time of surgery) were used in this study. Animals were housed individually on a 12-hour light/dark cycle. Some data included in this analysis were used in previous publications for different purposes 47,50 .

The Dome apparatus

The planetarium-style, virtual reality environment (the 'Dome') consisted of a hemispherical projection shell (2.3-m inner diameter) and an annular table (152.4-cm outer diameter and 45.7-cm inner diameter). The interior surface of the shell served as a projection screen. An annular ring was projected near the zenith throughout the session to provide illumination, and an array of visual landmarks was projected below it. The visual landmarks were stationary (epoch 1), rotated in response to the animal's movement (epochs 2 and 3) or disappeared (epoch 4), as detailed in the 'Experimental procedure' subsection.

The annular table, concentric with the shell, served as a onedimensional circular track for the animals. The animals were harnessed onto a radial arm via two three-dimensional printed arms; the radial arm was connected to a commutator placed in the center of the table. A liquid reward vial, pump and battery were mounted on the commutator drum. The displacement of the radial arm was monitored using an optical encoder. To mask auditory cues, white noise was played by a speaker underneath the table.

The experiment makes use of multiple frames of reference to control the visual scene. The lab frame is the location of the animal relative to the room, and the landmark frame is the location relative to the array of landmarks. A third frame of reference is the hippocampal frame, which is the location decoded from the activity of hippocampal place cells and will be discussed later (see the 'Hippocampal gain and the hippocampal frame of reference' subsection). The motion of the visual scenes was governed by the experimental gain, G, such that $G \times$ (displacement in lab frame) = (displacement in landmark frame). For instance, landmarks are stationary at G = 1, and landmarks move proportionally to the animal's movement in the same direction as the animal when G < 1 and in the opposite direction as the animal when G < 1.

Experimental procedure

After animals were trained to run counterclockwise in pursuit of a liquid reward (Yoo-hoo or 50% diluted Ensure) on a circular track, hyperdrives with six (two rats) or 12 (three rats) independently movable tetrodes were implanted. After surgery, tetrodes were advanced to the CA1 across days, and rats were trained inside the Dome to recover their running behavior. For the experimental sessions, a unity-gain headstage was connected to the hyperdrives, and the spiking $(600-6,000 \, \text{Hz})$ and the LFP $(1-475 \, \text{Hz})$ signals were digitized at $30 \, \text{kHz}$ and recorded through Cheetah 5 recording software (NeuraLynx). Rats ran counterclockwise in pursuit of the liquid reward that was provided at pseudorandom intervals (a uniform distribution with means $40-80^\circ$), pulling the radial arm with them, until they completed the required number of laps; the number of laps was determined based on the final experimental gain value.

For the first 1–3 sessions, landmarks were stationary (G=1) and were turned off after 30 laps. Subsequent sessions consisted of four epochs. In epoch 1, landmarks remained stationary (G=1), and the length varied across animals (four laps for rats 515 and 576, six laps for rats 637 and 638 and 15 laps for rat 692). In epoch 2, G gradually ramped up or down linearly until it reached the final gain value for epoch 3. The gain ramp rates ranged from 1/128 to 1/26 (gain change per lap). In epoch 3, G was maintained at the final gain value. The final gain values

were as follows: 0, 0.9375 and 1.0625 for rat 515; 0.25, 0.5, 0.9375, 1.5, 1.6 and 1.75 for rat 576; $1\pm n/13$ (n=2, 6 and 10) for the remaining animals. The values for the last three animals were chosen such that the position of the animal in the lab and the landmark seldom aligned (once every 13 laps). In addition, rat 637 had a session with $G_{\rm final}=0$, and rat 692 had two sessions with $G_{\rm final}=0.1$. In epoch 4, landmarks were turned off, and rats ran inside the Dome with only the spatially uninformative ring light. The sessions were ordered such that the same final gains did not repeat in consecutive days (other than a few exceptions) and that the gain deviance from 1 mostly increased over sessions. From the quantitative analyses, gain values were grouped into low (0.1–0.7), mid (0.7–1.3) and high (1.3–1.9) gain conditions.

Unit inclusion criteria

For all data analysis, MATLAB 2023b, as well as various MATLAB packages, was used. Sessions that contained epochs 1-4 were used in the analysis (a total of 51 sessions), excluding familiarization sessions and sessions that were terminated halfway due to poor behavior of the animal. For these sessions, spikes from each tetrode were sorted into units using custom software (WinClust; J.J.K.). Each cluster was assigned an isolation quality from 1 (very well isolated) to 5 (poorly isolated). The following procedure was used to define the units/spikes to be included in the quantitative analysis. First, we limited the analysis to putative pyramidal cells with good isolation quality (1-3). Units were classified as putative pyramidal cells using k-means clustering based on the firing rate, spike duration and autocorrelation ⁹⁴. Second, for units that passed the above criteria, spikes during immobile periods (movement speed <5° per second) were removed from the analysis. Third, to ensure that we were analyzing only units that displayed robust activity, each unit was required to fire a minimum of 50 spikes in a given epoch of interest to be included in the analysis, except for the following two analyses. For the landmark failure analysis, units with at least 50 spikes during landmark failure were included because the analyses did not segment the session into separate epochs. For the hippocampal gain decoding analysis, units with at least 50 spikes throughout the session were included, for the same reason that the analysis is agnostic to the epoch structure.

Hippocampal gain and the hippocampal frame of reference

To quantify the rate at which the animal updates its location in the hippocampal map, the hippocampal gain H (defined as the spatial frequency of place cell firing) was computed. For example, without any visual manipulation, H=1, meaning that a place cell with one place field on the track will fire at one location per lap. On the other hand, when the hippocampal map is locked to the moving landmarks, H=G; if G=2, the above cell will fire every 180° (twice per lap), whereas, when G=0.5, it will fire every two laps.

The hippocampal gain H was computed as follows. For each unit, the spatial frequency spectrogram was obtained using a window of 12 laps shifted every 5° . The spectrogram was sharpened through a reassignment procedure and thresholding. Finally, the maximum energy trajectory was extracted upon masking out harmonics of the fundamental frequency at each spatial bin. Once these unit-level hippocampal gain traces were yielded, the population-level hippocampal gain H was defined for each spatial bin as the median of all unit-level hippocampal gains. The hippocampal frame was defined as a reference frame that rotated with a gain value H. A session was defined as a landmark control session if the mean value of H/G during epochs 1-3 was 0.9-1.1, meaning that the hippocampal map was anchored to the landmarks. Sessions that passed this threshold were used for further analyses (except for the landmark failure analysis).

To quantify the coherence of the hippocampal population, we defined a coherence error score for each unit as the session median of $|1-H_i/H|$, where H_i is the gain of unit i and H is the median gain of the session computed with H_i excluded 47 . If the gains of individual place cells are nearly identical to each other, the error score should be close to 0.

Definition of place cells and place fields

All subsequent analyses were limited to cells that were classified as place cells. To this end, the spatial information (SI) score⁹⁵ was computed for each cell in the landmark frame as

$$\sum_{i=1}^{N} p_i \frac{\lambda_i}{\lambda} \log_2 \frac{\lambda_i}{\lambda}$$

where p_i is the occupancy probability of the animal in bin i; λ_i is the firing rate in bin i; and λ is the mean firing rate. Units with (1) SI \geq 0.7 and (2) $SI \ge 95\%$ of circular shifted SIs during epochs 1–3 were defined as place cells. Here, the circular shifting procedure was performed as a statistical test that preserved the temporal structure of spike trains; the shifting procedure can decouple the temporal structure of the spike train from the animal's position when the trajectory is highly variable (for example, open arena). However, the animals in our task ran on a circular track at relatively regular speeds, yielding regularized trajectories; as a result, simple shifting more likely retained the coupling of the spike train and the animal's position. To reduce such spurious place tuning, we first inverted the spike train in time; for instance, spikes emitted at the beginning of the session were now assigned to the end of the session %. Shifts were then set every 0.5 seconds starting from 15 seconds after the beginning of the session until 15 seconds before the end of the session. For epoch 4 and landmark failure sessions, place cells were defined separately using the hippocampal frame to compute the SIs, because there was no external frame to which the place cell firing was locked.

To define place fields, the circular position in the landmark frame was quantized into 1° bins. To create a place tuning curve for each epoch, the number of spikes was divided by the time spent by the animal in each bin, both smoothed using a circular kernel density estimation (Gaussian kernel width = 4°). Place fields were defined from the tuning curve as consecutive bins of at least 25° in size whose firing rate was at least 10% of the maximum firing rate. To avoid artificial splitting of fields when the firing rate fell below the threshold for short intervals, fields that were closer than 10° were concatenated 9798 .

To control for the subtle yet continuous shift in the field position relative to landmarks that often occurred during gain manipulation for example, the slow drift in the place field location in the landmark frame between laps 30 and 80 in Fig. 1e), we defined lap-based fields by assigning the first and the last spike that occurred within the lap-averaged field for a given lap as the start and the end of the field, similar to ref. 80. Lap-based fields were defined only for laps with at least three spikes. The lap-based place field size was defined as the median of the lap-based firing range (distance between the first and last spikes) across laps. For field-based analyses, fields with at least 50 spikes were included in the analysis. Because of remapping events during gain manipulation 7, place fields in epochs 1 and 3 were treated as independent data points. For epoch 4 and landmark failure sessions, place fields were defined in the hippocampal frame of reference.

LFP extraction

For each experimental session, the tetrode with the strongest mean theta power was used to extract the theta components using a 6–12-Hz bandpass Butterworth filter. The Hilbert transform was applied to the signal to obtain the phase and amplitude of theta components. To account for differences in theta phase depending on the recording sites and to allow comparison across sessions and animals, zero phase was defined for each recording session as the phase with maximal CA1 pyramidal cell activity. In two of the sessions, owing to the poor sampling of cells, the estimated zero phase seemed to be 180° offset (as judged by the position—phase plot of phase precession). For these two sessions, this phase offset was manually corrected. The correction d id not qualitatively change the results reported here. Gamma components of the LFP were extracted by band-passing the signal from 30 Hz to 240 Hz and applying a continuous wavelet transform (31 Morlet

wavelets with logarithmically equidistant frequencies in the range specified above).

Theta modulation modality of place cells

Although many place cells in the hippocampus preferentially fire at the trough of the local theta oscillation in the stratum radiatum, thus exhibiting unimodality, some cells exhibit bimodality, also firing at the peak. The second peak arises in deep-layer cells due to increased innervation from ECIII (ref. 100). To categorize these two types of place cells, we defined the modality of place cells by the number of peaks in the theta phase preference histogram. The theta phase preference histogram was created by compiling the LFP theta phase at which spikes occurred during mobility in epochs 1 and 3. First, theta modulation was tested against a uniform phase distribution (Hermans-Rasson test, P < 0.05). Note that the use of the Hermans–Rasson test allows for the detection of a multimodal distribution, in contrast to the circular Rayleigh test that assumes a von Mises distribution 101. All units passed the test. To characterize the modality of theta modulation, a smoothed phase preference curve was created using circular kernel density estimation (bin width = 10°, Gaussian kernel width = 12°). The firing rate index³⁷ was obtained from this smoothed histogram by first dividing the values by the maximum value and then subtracting the minimum value of the resulting histogram. Peaks of the histogram were included in the analysis if they met the following criteria: peak prominence \geq 0.05, peak height \geq 0.3 × (max peak height), peak distance \geq 50° and peak width ≥30°. Units with one peak and two peaks were classified as unimodal and bimodal units, respectively. Units with more than two peaks were left unclassified.

Quantification of phase precession

For each place field, the relationship between the normalized position and theta phase for the spikes was visualized (for example, Fig. 1a). A small number of precessions showed doublets, where a single field contained two precessions, presumably due to two fields that were adjacent to each other 11,52; these doublets (n=10) were removed from further analyses. To characterize the position–phase relationship, we obtained the slope as a first-order structure parameter using circular–linear regression 53. The analysis allows us to treat position as a linear variable and theta phase as a circular variable. In brief, for the mean resultant length R defined as

$$R = \sqrt{\left[\frac{1}{n}\sum_{j=1}^{n}\cos(\phi_{j} - 2\pi ax_{j})\right]^{2} + \left[\frac{1}{n}\sum_{j=1}^{n}\sin(\phi_{j} - 2\pi ax_{j})\right]^{2}},$$

the slope \hat{a} was defined as the parameter a that maximized R with range restricted from -4π to 4π . Two additional parameters, the phase offset and correlation coefficient, were also computed. The phase offset was derived as

$$\hat{\phi}_0 = \arctan \frac{\sum_{j=1}^{n} \sin(\phi_j - 2\pi \hat{a}x_j)}{\sum_{j=1}^{n} \cos(\phi_j - 2\pi \hat{a}x_j)}.$$

The circular-linear correlation coefficient was computed as

$$\hat{\rho}_c = \frac{\sum_{j=1}^n \sin(\phi_j - \bar{\phi})\sin(\theta_j - \bar{\theta})}{\sqrt{\sum_{i=1}^n \left[\sin(\phi_i - \bar{\phi})\right]^2 \sum_{j=1}^n \left[\sin(\theta_j - \bar{\theta})\right]^2}}$$

where $\theta_j = 2\pi |\hat{a}| x_j \pmod{2\pi}$ and $\bar{\phi}$ and $\bar{\theta}$ are circular sample means. Parameters for single-traversal statistics were computed similarly using spikes from each lap separately.

To quantify phase precession during epoch 4 and landmark failure sessions, where the place cell firing was not locked to either the landmark or the lab frame, circular–linear regression was performed with

position based on the hippocampal frame. The mean hippocampal gain during the epoch was used as the gain experienced by the cell. Equivalent analysis was done for landmark failure sessions, except that only landmark failure traversals (H/G > 1.1 or H/G < 0.9) were used. One of the landmark failure sessions had a hippocampal gain locked to the lab frame, potentially due to residual local cues and, thus, was eliminated from the analysis.

Spike phase spectrum analysis

To quantify the theta-modulated firing frequencies of cells, we used spike phase spectrum analysis. The analysis is similar to standard spectral analyses, except that the frequency is defined in relation to the LFP theta phase and not time. This modification allows for quantification of the difference in theta-modulated place cell firing and the LFP theta frequency while allowing for the theta frequency to change over time. In this analysis, a spike frequency of 1 corresponds to a firing locked to the theta rhythm, whereas a value greater than 1 corresponds to spike bursts occurring faster than the LFP (phase precession).

To compute the spike phase spectrum, the LFP theta phase was first unwrapped such that the phase monotonically increased with time. A spike train was constructed by binning the LFP theta every $\pi/90$. The power spectrum was computed from the spike train via Thomson's multi-taper power spectral density estimate using Slepian tapers with a time-half-bandwith product of 4. The resulting spectrum was smoothed with a Gaussian kernel (kernel width = 100 bins), and the theta-modulated peak was defined as the peak frequency between 0.7 and 1.3. Prominent theta peaks were defined as those whose mean power around the peak (width of 0.05) was larger than double the mean power between 0.5 and 0.7 and between 1.3 and 1.5 (ref. 57). Fields with prominent theta-modulated peaks were included in the analysis. Raw precession rate was defined as the peak frequency from the spike phase spectrum – 1. Because the spectral analysis requires that the animal is $running\ continuously, only\ sessions\ with\ good\ running\ behavior\ (mean$ speed ≥20° per second) were included.

Burst frequency is known to be modulated by the field size and the animal's running speed¹⁶. To isolate the effect of gain on the theta-modulated firing properties, we computed an NPR, defined as (raw precession rate) × (field size in landmark frame) × (mean theta frequency) / (mean animal speed). This index was derived as follows. The time it takes for the animal to traverse through a field is given as (field size in landmark frame) / (animal speed in landmark frame). At the same time. the time to complete a full precession is 1/((raw precession rate) × (theta frequency)) assuming linear precession. By equating the two terms and using the fact that (animal speed in landmark frame) = (animal speed) \times *G*, we obtain (raw precession rate) \times (field size in landmark frame) \times (mean theta frequency) / (mean animal speed) = G, or NPR = G. Thus, under the assumption of linear precession that extends a full theta cycle, NPR should scale linearly with gain at a slope of 1. Three outlier units (NPR < -3) were removed from the analysis when estimating the slope, but this exclusion did not significantly alter the results. Note that multiplying the precession rate by the mean theta frequency is different from taking the difference between the mean burst frequency and the mean theta frequency because the former is a more sensitive measure if the bursting and LFP theta frequencies vary over time within a session. Results held using the raw precession rate. Spike phase spectrum analysis for the forward/reverse windows was done similarly but only using spikes that occurred in the respective theta phase ranges and only using cells that showed prominent theta peaks in both windows.

Theta compression

Theta phase precession is associated with the formation of forward theta sequences, where a sequence of place cell firing is reinstantiated within a single theta cycle 19,20 . To quantify this theta compression, the CF was computed as follows. First, among place cells with single place fields, we selected pairs of place cells with overlapping fields (overlap

≥10°; pairs where one field was engulfed in the other were excluded) and similar place field sizes ((larger field size) / (smaller field size) < 2). Second, for each place field pair, a CCG was computed with 5-ms bins, followed by a Gaussian smoothing (kernel width = 50 ms). Third, the theta-scale time lag was computed as the highest peak of the CCG within 125 ms (or -125 ms, depending on the spatial sequence of place fields traversed by the animal). Previous studies showed that when theta sequences are observed in a given theta cycle, cells with nearby place fields fire closely in time, resulting in the CCG peaking around 0; on the other hand, place cells with fields that are further apart fire with a larger temporal delay, producing a larger offset of the CCG peak¹⁹. CCGs that did not have a peak in this range or with the largest peak in the opposite sign compared with predicted were excluded from this analysis. Lastly, CF was defined as the ratio between the theta-scale time lag and the distance between the center-of-mass of the two place fields in the landmark frame.

Quantifying burst and theta skipping dynamics

To compute the burst dynamics, spikes that occurred within 6 ms of another spike were considered a part of burst firing, whereas spikes that $did\,not\,belong\,to\,bursts\,were\,treated\,as\,isolated\,spikes^{100,102}.\,Bursting$ rate was defined as the number of bursting events relative to all events (bursts and isolated spikes). To quantify 'theta missing', theta-missing index was defined as the rate of inter-burst intervals (IBIs) that were greater than 1/6 seconds. To ensure that we were not including long IBIs due to intermittent pausing, we excluded IBIs that were greater than 1 second. The inclusion of all IBIs within a traversal did not change the result qualitatively. To quantify the rate of alternate theta skipping, where cells fire at every other theta cycle, autocorrelograms (ACGs) were computed with a 5-ms bin, smoothed with a Gaussian kernel (kernel width = 50 ms) for cells with single fields^{24,59}. If a cell spikes every theta cycle, the corresponding ACG will exhibit a high peak at around 125 ms together with lower peaks at its harmonics (250 ms, 375 ms and so on). On the other hand, if the cell systematically fires at every n-th cycle, the ACG will exhibit high peaks at around $125 \times n$ ms. The theta-modulated peak (peak 1) was defined as the highest peak between 1/12 seconds and 1/6 seconds and peak 2 as the highest peak in the range 1/6-1/3 seconds. From these peaks, the theta skipping index was computed as (peak 1 – peak 2) / max(peak 1, peak 2).

Quantifying the two-lobe structure

To examine whether the occupancy of spikes in position—phase space differs between positive-slope and negative-slope traversals, we compiled spikes that belong to one of the two types of traversals. Each spike was convolved with a Gaussian kernel for smoothing, and the overall position—phase plot was normalized. The two resulting smoothed precession plots were subtracted from each other to visualize the subspace within the position—phase space that was occupied more by negative-slope traversals than positive-slope traversals (and vice versa).

To quantify the prominence of phase procession, we first assigned each spike to one of the two lobes by using the phase range that was previously reported to show forward (-110° to 60°) and reverse ($80-230^{\circ}$) theta sequences ³⁷. Forward and reverse theta sequences emerge from phase precession and procession, and the phase ranges matched the range at which the two lobes were observed in our data (Fig. 5d). Using these two phase ranges, the SLI was defined as the proportion of the spikes in the reverse window; the larger the value is, the phase code contains a stronger processing component. SLI was computed for individual traversals, and the median SLI value for each cell was used for the analysis.

Several control analyses were done to test if the change in the SLI can be explained away by factors other than gain. To control for the difference in theta frequency, we binned the traversals based on the mean theta frequency of the traversal (bin width = 0.5 Hz), and the SLIs were randomly shuffled within each frequency bin (Extended Data Fig. 5a). We recomputed the SLI of each cell using these shuffled values, and the

median SLIs for each of the four gain groups (epoch 1, low, mid and high) were obtained. This shuffling process was performed 1,000 times, and the P value was computed by comparing the difference in median SLI values from epoch 1 and the low/mid/high groups against the true difference. To strictly enforce equal sampling of theta frequencies, median SLI values were computed only using frequency bins that were sampled by all four groups. Similar shuffling analyses were done for traversal distance through the fields in the lab frame (bin width = 30°), animal's mean speed (bin width = 10° per second), time passed since the start of the experiment (bin width = 100° seconds) and theta modulation modality. Note that, for the shuffling in time, only epoch 3 was used because epochs 1 and 3 were by definition separated in time.

Theta-gamma coupling/spike-LFP coupling

To visualize gamma components coupled to the underlying theta rhythm, we used an unsupervised clustering algorithm developed by Zhang et al. 103. In short, a frequency and theta phase power (FPP) matrix was computed for each theta cycle using the LFP signal. A k-means clustering algorithm was employed to detect groups of pixels whose power was co-modulated across theta cycles. The detected components were then ranked in the order of central frequency, and the first two components were labeled as slow and medium gamma (Extended Data Fig. 7a). Note that the frequency ranges of these components match previous literature^{68,103}. For each session, gamma components were extracted by averaging over the components extracted from tetrodes that contained place cells. The resulting components showed the slow gamma component in approximately 20-60 Hz and the medium gamma component in approximately 70–140 Hz. Spike-LFP coupling analysis was limited to frequency ranges higher than 30 Hz to avoid the leakage of theta harmonics104.

To measure how the spiking activity is locked to the underlying LFP, spike-LFP coupling was computed using the mean resultant length (MRL) of phases of each frequency. Spike-LFP coupling measures are known to suffer from two issues. First, spectral contents of individual spikes can contaminate the LFP even down to 50 Hz¹⁰⁵⁻¹⁰⁷. Such spectral leakage can lead to spurious spike-LFP coupling. Second, MRL is highly sensitive to the number of spikes used for the analysis 108. To address these issues, the spike-LFP coupling indices were computed for each cell as follows. First, among all tetrodes that contained place cells, the tetrode that contained the cell of interest was excluded from the analysis to minimize spike leakage. Second, for each of the remaining tetrodes. MRL was computed for each frequency component of the LFP. Here, the spikes were randomly downsampled to 50 before computing the MRL, addressing the issue of spike number dependence of MRL. This procedure was performed 50 times, and the maximum value of the mean MRL across tetrodes was taken as the spike-LFP coupling index of the cell. Mean spike-gamma coupling values during the G = 1 condition for each frequency were subtracted to obtain the baseline-subtracted spike-LFP coupling. Peak values of the resulting spike-LFP coupling strength in slow and medium gamma frequency ranges for each cell were used for analysis.

Continuous ring attractor model

To address a potential mechanism that gives rise to the observed result, we adopted a CAN model of Chu et al. ⁴⁴ that reproduced a behavior akin to theta phase precession and procession ^{109,110}. The model consists of a CAN with the addition of feedback inhibition connections to each node that destabilizes the activity bump. The CAN framework is constructed such that each node x represents a place field, and the synaptic input received by the corresponding place cell and its activity level are denoted as U(x,t) and r(x,t), respectively. The nodes send recurrent connections to each other, denoted as J(x,x'), where fields closer to each other send stronger excitations, typical of CAN models. Here, the connectivity is modeled as a ring attractor to mimic the circular track used in the Dome. When an external excitatory input

 $I_{\rm ext}(x,t)=I_{\rm allo}(x,t)+I_{\rm idio}(x,t)$ is applied, the recurrent connection allows for the formation of a stable Gaussian activity bump centered around node x under coherent allothetic and idiothetic inputs. However, each node also receives a feedback inhibition component V(x,t), which destabilizes the activity bump. In a certain regime between the balance of excitatory and inhibitory inputs, the network exhibits oscillatory tracking, where the activity bump oscillates around the external excitatory input. Under this state, the activity of each node was shown to exhibit phase precession and procession relative to the network oscillation. During experimental gain manipulation, the speed of the allothetic input was faster (or slower) than the idiothetic input by a factor of G. In such cases of incoherence in allothetic and idiothetic inputs to the network, the idiothetic input was periodically aligned to the allothetic input (every D (m) of movement in the idiothetic frame) to account for the influence of landmarks to correct for cumulative path integration error $^{74-76}$.

More formally, the dynamics of the CAN model can be described as follows:

$$\tau \frac{dU(x,t)}{dt} = -U(x,t) + \rho \int_{-\pi}^{\pi} J(x,x') r(x',t) dx' - V(x,t) + I_{ext}(x,t)$$

$$\tau_{v} \frac{dV(x,t)}{dt} = -V(x,t) + mU(x,t)$$

$$J(x,x') = \frac{J_{0}}{\sqrt{2\pi}a} \exp\left(-\frac{(x-x')^{2}}{2a^{2}}\right)$$

$$r(x,t) = \frac{gU(x,t)^{2}}{1 + k\rho \int_{-\pi}^{\pi} U(x',t)^{2} dx'}$$

$$I_{i}(x,t) = \alpha_{i} \exp\left[-\frac{(x-v_{i}t)^{2}}{4a^{2}}\right] \text{ for } i = \text{allo, idio}$$

where the description of each parameter can be found in Supplementary Table 3. Note that the synaptic input U(x,t) and the activity level r(x,t) are related via divisive normalization. From the resulting simulation, the theta phases at each timepoint were obtained via linear interpolation between the peaks and troughs of the network oscillation. For a detailed analysis of the model, refer to Chu et al. 38.

Statistics

Linear mixed-effects models (LMEMs) were used for most analyses unless stated otherwise. Here, the response variable (for instance, field size) was modeled with a group variable (for instance, gain group) as a fixed effect and rat ID and session ID as random effects. When comparing more than two groups, a Wald test was first used to assess whether there was an overall effect of the group variable; if significance was found, the t-statistics of each group pair comparison were reported. In cases where each unit contributed two data points (Fig. 5e-i), unit ID was added as an additional random effect to account for the paired data.

For phase offsets, hierarchical bootstrapping was used, because the circular nature of phase is incompatible with a simple LMEM. First, five rats were randomly sampled with replacement from the five rats in the original dataset. Second, for each sampled rat i,k sessions were randomly sampled with replacement, where k equaled the number of sessions from rat i. Third, circular means were computed for each gain group from this bootstrapped sample, and the circular distances between gain groups were obtained. Lastly, this procedure was performed 1,000 times, and the significance of the observed circular differences was assessed by computing the two-tailed P values using the bootstrapped distribution.

The Pearson correlation was used to test for the relationship between epoch-based and lap-based fields. The *F*-test against a

constant model was used to test for the significance of a correlation. The two-sample Kuiper test was used to compare the shape of the distribution of phase offsets for single-traversal phase coding statistics, accounting for the circularity of the variable. The chi-squared (χ^2) test was used to test for differences in proportions. Outlier points were removed in some plots (Figs. 3f and 5g and Extended Data Fig. 7b) for visualization purposes but were included in all statistical analyses unless stated otherwise. Each data point corresponds to individual units unless specified otherwise. The reported P values are false discovery rate (FDR) corrected for multiple comparisons when omnibus tests (for example, Wald test) are not applicable: *P < 0.05, **P < 0.01, ***P < 0.001; NS, not significant.

Reporting summary

Further information on research design is available in the Nature Portfolio Reporting Summary linked to this article.

Data availability

Preprocessed data used to perform the analyses and generate the figures in this paper are available via OSF at https://osf.io/nq65k/?. Source data are provided with this paper.

Code availability

The code is available via OSF at https://osf.io/nq65k/?.

References

- Csicsvari, J., Hirase, H., Czurkó, A., Mamiya, A. & Buzsáki, G.
 Oscillatory coupling of hippocampal pyramidal cells and interneurons in the behaving rat. J. Neurosci. 19, 274–287 (1999).
- Skaggs, W., McNaughton, B. & Gothard, K. An informationtheoretic approach to deciphering the hippocampal code. In Advances in Neural Information Processing Systems 5 (1992); https://proceedings.neurips.cc/paper_files/paper/1992/ hash/5dd9db5e033da9c6fb5ba83c7a7ebea9-Abstract.html
- Monaco, J. D., Rao, G., Roth, E. D. & Knierim, J. J. Attentive scanning behavior drives one-trial potentiation of hippocampal place fields. *Nat. Neurosci.* 17, 725–731 (2014).
- Mehta, M. R., Barnes, C. A. & McNaughton, B. L.
 Experience-dependent, asymmetric expansion of hippocampal place fields. Proc. Natl Acad. Sci. USA 94, 8918–8921 (1997).
- Lee, I. & Knierim, J. J. The relationship between the field-shifting phenomenon and representational coherence of place cells in CA1 and CA3 in a cue-altered environment. *Learn. Mem.* 14, 807–815 (2007).
- 99. Lubenov, E. V. & Siapas, A. G. Hippocampal theta oscillations are travelling waves. *Nature* **459**, 534–539 (2009).
- 100. Mizuseki, K., Diba, K., Pastalkova, E. & Buzsáki, G. Hippocampal CA1 pyramidal cells form functionally distinct sublayers. *Nat. Neurosci.* 14, 1174–1181 (2011).
- Landler, L., Ruxton, G. D. & Malkemper, E. P. Circular data in biology: advice for effectively implementing statistical procedures. *Behav. Ecol. Sociobiol.* 72, 128 (2018).
- 102. Ranck, J. B. Studies on single neurons in dorsal hippocampal formation and septum in unrestrained rats: part I. Behavioral correlates and firing repertoires. *Exp. Neurol.* **41**, 462–531 (1973).
- 103. Zhang, L., Lee, J., Rozell, C. & Singer, A. C. Sub-second dynamics of theta-gamma coupling in hippocampal CA1. eLife 8, e44320 (2019).
- 104. Igarashi, K. M., Lu, L., Colgin, L. L., Moser, M.-B. & Moser, E. I. Coordination of entorhinal-hippocampal ensemble activity during associative learning. *Nature* **510**, 143–147 (2014).
- 105. Liu, J. & Newsome, W. T. Local field potential in cortical area MT: stimulus tuning and behavioral correlations. J. Neurosci. 26, 7779–7790 (2006).

- 106. Ray, S., Crone, N. E., Niebur, E., Franaszczuk, P. J. & Hsiao, S. S. Neural correlates of high-gamma oscillations (60–200 Hz) in macaque local field potentials and their potential implications in electrocorticography. *J. Neurosci.* **28**, 11526–11536 (2008).
- Scheffer-Teixeira, R., Belchior, H., Leão, R. N., Ribeiro, S. & Tort, A. B. L. On high-frequency field oscillations (>100 Hz) and the spectral leakage of spiking activity. J. Neurosci. 33, 1535–1539 (2013).
- 108. Vinck, M., van Wingerden, M., Womelsdorf, T., Fries, P. & Pennartz, C. M. A. The pairwise phase consistency: a bias-free measure of rhythmic neuronal synchronization. *Neuroimage* 51, 112–122 (2010).
- 109. Folias, S. E. & Bressloff, P. C. Breathing pulses in an excitatory neural network. *SIAM J. Appl. Dyn. Syst.* **3**, 378–407 (2004).
- Folias, S. E. Nonlinear analysis of breathing pulses in a synaptically coupled neural network. SIAM J. Appl. Dyn. Syst. 10, 744–787 (2011).
- 111. Fenton, A. A. & Muller, R. U. Place cell discharge is extremely variable during individual passes of the rat through the firing field. *Proc. Natl Acad. Sci. USA* **95**, 3182–3187 (1998).
- Madhav, M. S. et al. Control and recalibration of path integration in place cells using optic flow. *Nat. Neurosci.* 27, 1599–1608 (2024).
- 113. Lopes-Dos-Santos, V. et al. Parsing hippocampal theta oscillations by nested spectral components during spatial exploration and memory-guided behavior. *Neuron* **100**, 940–952 (2018).

Acknowledgements

We thank F. P. Battaglia for feedback on an earlier version of the paper, S. Zeger for statistical consultation and H. T. Blair and the members of the Cowan and Knierim laboratories for helpful comments. This research was supported in part by National Institutes of Health grants RO1 NS102537 (J.J.K., N.J.C. and F.S.), RO1 MH118926 (J.J.K. and N.J.C.) and R21 NS095075 (J.J.K. and N.J.C.); the Johns Hopkins Kavli Neuroscience Discovery Institute (M.S.M.); the Masason Foundation (Y.S.); the Ezoe Memorial Recruit Foundation (Y.S.); the Quad Fellowship (Y.S.); and the Honjo International Scholarship Foundation (Y.S.).

Author contributions

R.P.J., M.S.M., F.S., N.J.C. and J.J.K. conceived of the study. All authors designed the analyses. Y.S. performed the formal analysis. Y.S. and J.J.K. wrote the paper, with input from all authors. N.J.C. and J.J.K. supervised the project.

Competing interests

The authors declare no competing interests.

Additional information

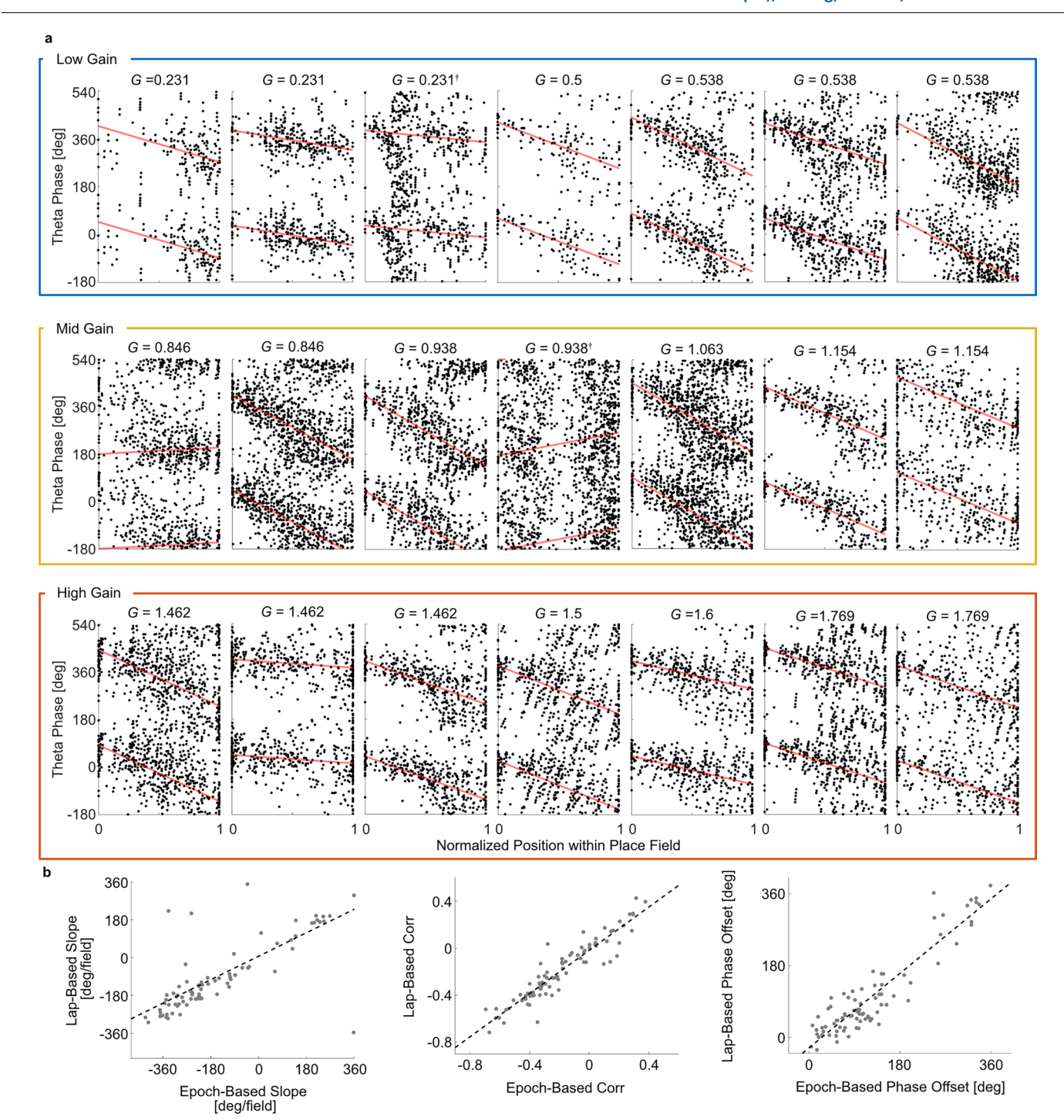
Extended data is available for this paper at https://doi.org/10.1038/s41593-025-02038-6.

Supplementary information The online version contains supplementary material available at https://doi.org/10.1038/s41593-025-02038-6.

Correspondence and requests for materials should be addressed to James J. Knierim.

Peer review information *Nature Neuroscience* thanks Michael Hasselmo and the other, anonymous, reviewer(s) for their contribution to the peer review of this work.

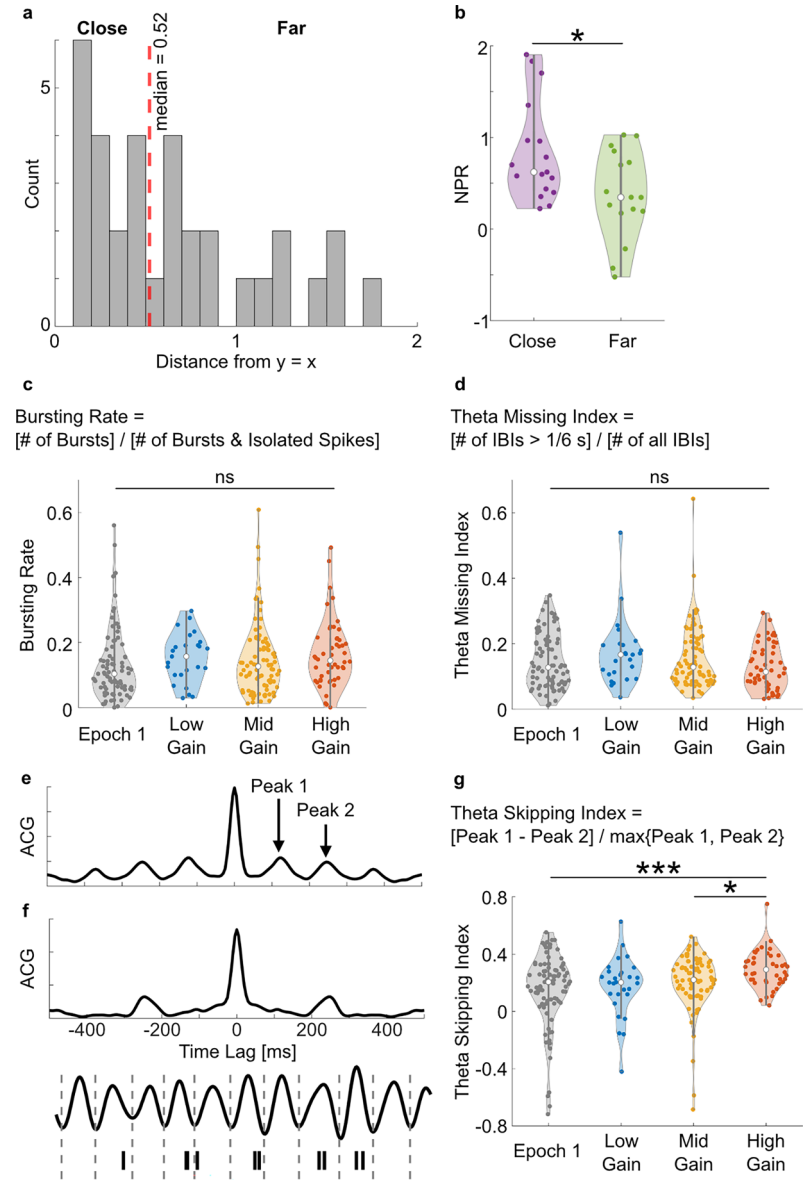
Reprints and permissions information is available at www.nature.com/reprints.



$\label{lem:extended} \textbf{Extended Data Fig. 1} | \textbf{Characterization of phase precession inside the Dome.}$

a, Example position–phase plots in landmark frame with different values of *G*. Red lines indicate the best-fit lines of the precession, computed using circular-linear regression. Place fields that contained double precessions are indicated by daggers and were excluded from further analyses. **b**, Comparison of precession statistics in epoch-based vs. lap-based fields. Epoch-based fields were defined from the tuning curve of the place cell during the entire epoch, while lap-based fields were defined as the range within the epoch-based field that the cell fired in a given lap. The lap-based field accounts for the lap-to-lap variability of the firing field locations. This is especially important in this dataset, since the gain manipulation often caused a slight but continuous drift of the field locations throughout the session, making the epoch-based field larger than typical individual passes through the field. To test that our definition of

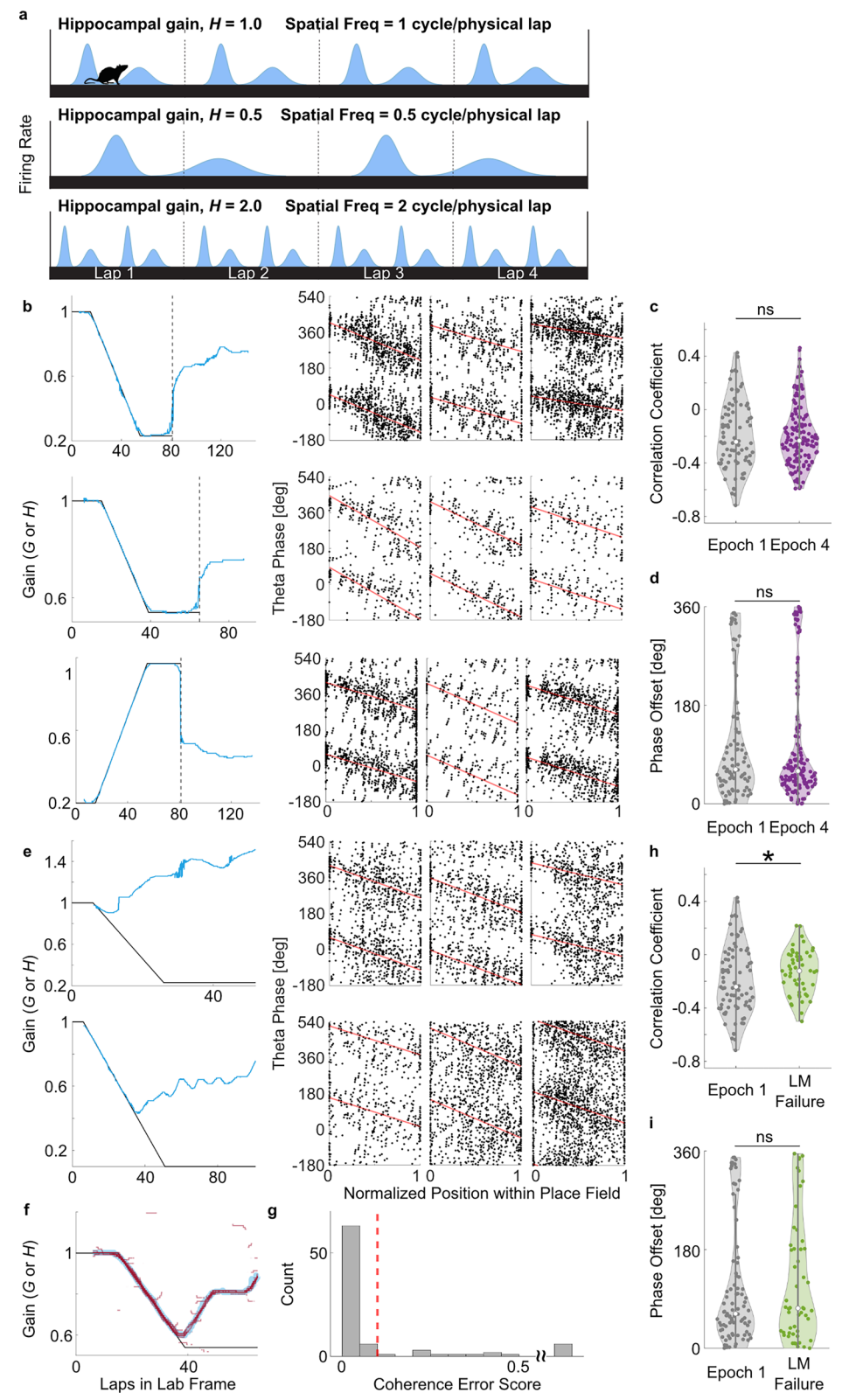
lap-based fields produced a position—phase plot consistent with a more standard epoch-based field definition when fields did not have a biased drift, we compared the statistics of precession using data from epoch 1. Lap-based definition of place fields did not affect the correlational structure of phase coding but shallowed the slope estimate. Left, Precession slope. Best fit line: y=0.622x+6.33 (rho=0.753, $P=1.00\times10^{-16}$). Middle, Correlation coefficient. Best fit line: $y=0.919x\cdot0.0189$ ($rho=0.935, P=4.44\times10^{-39}$). Right, Phase offset. Best fit line: y=1.04x-26.5 ($rho=0.709, P=8.64\times10^{-9}$). Since the phase offset is a circular variable, the best fit line was found after wrapping around each lap-based phase offset such that the difference with its epoch-based counterpart was less than 180 degrees. Moreover, the correlation coefficient and the P value were computed using a circular-circular regression.



Extended Data Fig. 2 | Scaling in the theta-modulated bursting frequency is accompanied by changes in other theta-modulated firing properties.

a-b, Change in NPR is predicted by the unit's initial NPR. **a**, Histogram of the y-coordinate distance between each unit's NPR in epoch 3 and the y = x line. A distance of 0 means that the unit scaled its theta-modulated firing frequency perfectly with gain. The units that formed fields in both epochs 1 and 3 were classified as having NPRs close to (distance < median) or further from (distance > median) the theoretical value. **b**, NPR of the two groups in epoch 1 (n = 33 units). Units that scaled their theta-modulated firing frequencies more faithfully in epoch 3 tended to have higher NPRs in epoch 1. β = 0.461, s.e. = 0.174, t(31) = 2.65, P = 0.0125; t-statistics/two-sided P value from the LMEM. Each violin plot shows the median (white circle), IQR (gray line), and distribution outline. **c**, Bursting rate was invariant to gain (n = 246 units). Overall: W(3) = 5.25, P = 0.154 (two-sided); Wald test on the LMEM. **d**, Theta-missing index was invariant to

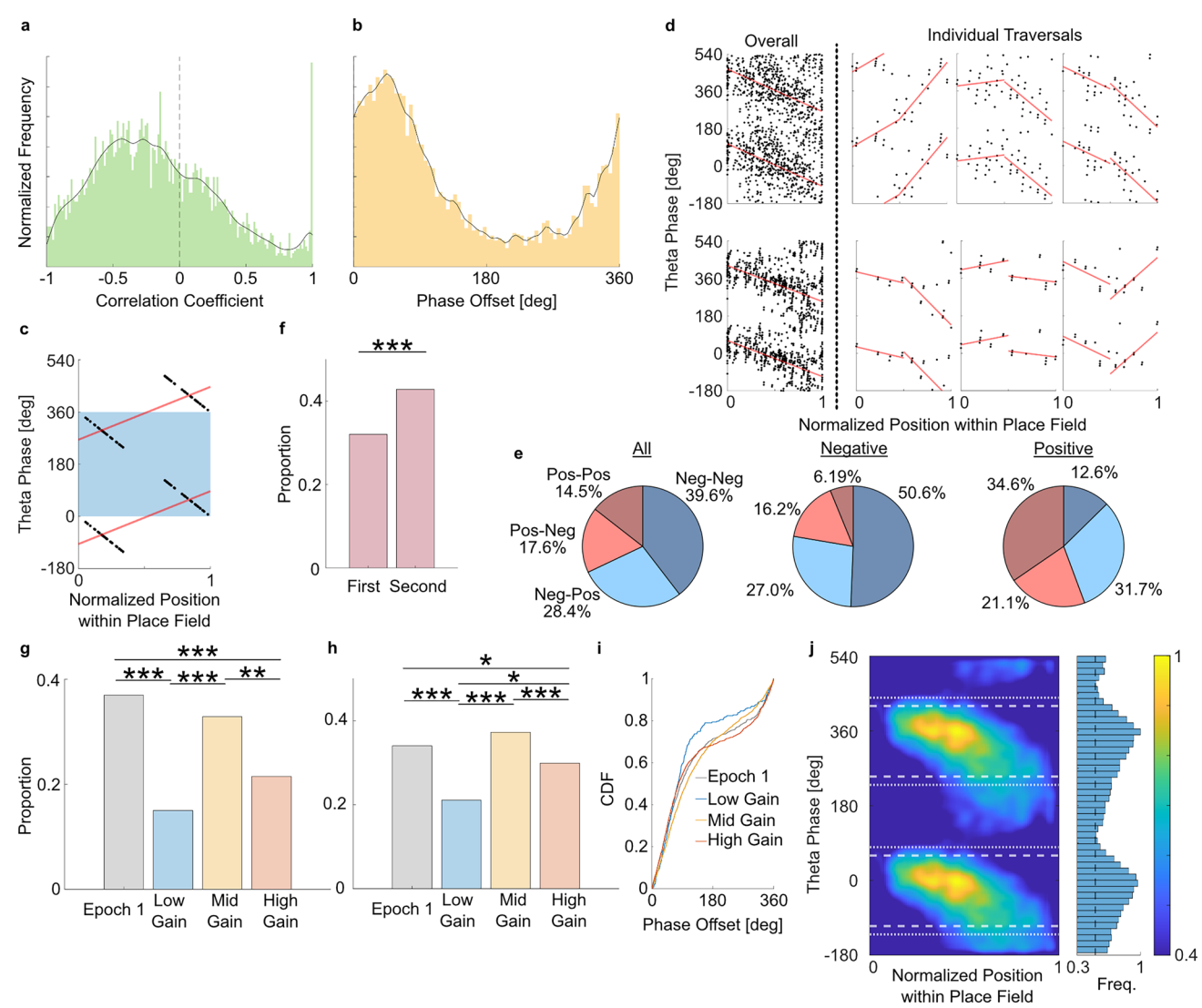
gain (n = 246 units). Overall: W(3) = 2.75, P = 0.432 (two-sided); Wald test on the LMEM. **e**-**g**, Quantification of theta-skipping^{24,58-60}. **e**, Autocorrelogram (ACG) of an example unit without theta-skipping. **f**, Top, ACG of an example unit with theta-skipping. Note the disappearance of peak 1. Bottom, spiking of this unit relative to theta. **g**, Theta-skipping index was higher (less theta-skipping) in high gain condition compared to mid gain and G = 1 conditions (n = 242 units). Overall: $W(3) = 14.6, P = 2.17 \times 10^{-3}$ (two-sided); Epoch 1 vs. Low: $\beta = -0.0808$, s.e. = 0.0500, t(238) = -1.62, P = 0.107, Epoch 1 vs. Mid: $\beta = -0.0438$, s.e. = 0.0304, t(238) = -1.44, P = 0.150, Epoch 1 vs. High: $\beta = -0.146$, s.e. = 0.0408, $t(238) = -3.59, P = 3.98 \times 10^{-4}$, Low vs. Mid: $\beta = 0.0370$, s.e. = 0.0552, t(238) = 0.671, P = 0.503, Low vs. High: $\beta = -0.0656$, s.e. = 0.0601, t(238) = -1.09, P = 0.276, Mid vs. High: $\beta = -0.103$, s.e. = 0.0458, t(238) = -2.24, P = 0.0259; Wald test followed by t-statistics/two-sided P values from the LMEM. *: P < 0.05, ***: P < 0.001.



Extended Data Fig. 3 | See next page for caption.

Extended Data Fig. 3 | Quantification of theta phase coding in the absence of landmarks and under conditions of failure of landmark control. a, Schematic of the hippocampal gain. When the pattern of place cell firing repeats every physical lap, the hippocampal map is locked to the lab frame (H = 1). Under gain manipulation, the same pattern repeats every n laps ($n \ne 1$), which is defined as a hippocampal gain of 1/n. Reproduced from 112. b, Example gain traces for epochs 1 through 4 and respective position—phase plots in epoch 4. The black (G) and blue (H) lines overlap during epochs 1–3, demonstrating the strong control of the hippocampal map by the landmarks. In epoch 4, the blue traces were maintained at values different from 1, demonstrating path integration gain recalibration 47. c, Circular-linear correlation coefficients for epochs 1 and 4 (n = 233 units). β = 0.0148, s.e. = 0.0305, t(231) = 0.485, P = 0.628; t-statistics/two-sided p-value from the LMEM. Each violin plot shows the median (white circle), IQR (gray line), and distribution outline. d, Phase offsets for epochs 1 and 4 (n = 233 units).

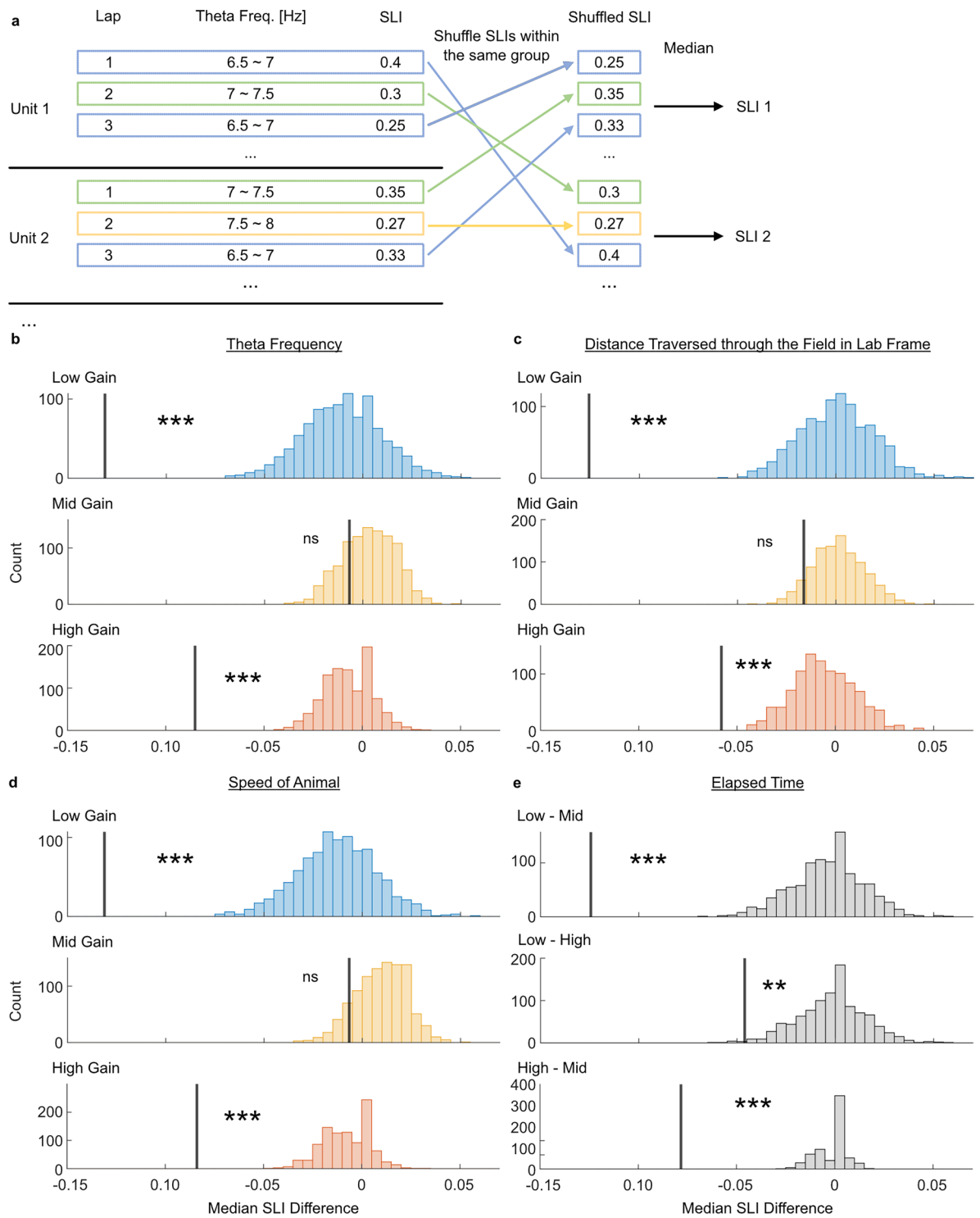
P=0.556 (two-sided); hierarchical bootstrap test. **e**, Example gain traces of landmark failure (LMF) sessions and respective position–phase plots during LMF. The blue line (H) dissociated from the black line (G) during epochs 2 and 3. **f**, Example gain traces of an LMF session from individual place cells. The thick blue line (H) and the red lines (unit gains) overlap, demonstrating the coherence of the hippocampal map. **g**, Coherence error score of all place cells recorded during LMF as reported in Fig. 2g of 17 . The dashed line indicates a coherence error score of 0.1, analogous to the threshold defining landmark control. Most place cells (69/85) exhibited error scores < 0.1, indicating the coherence of the hippocampal population. Units with coherence error scores > 0.5 were grouped into a single bin. **h**, Circular-linear correlation coefficients for epoch 1 and LMF (n=137 units). $\beta=0.0816$, s.e. =0.0397, t(135)=2.05, P=0.0419; t-statistic/two-sided P value from the LMEM. **i**, Phase offsets for epoch 1 and LMF (n=137 units). P=0.802 (two-sided); hierarchical bootstrap test. *: P<0.05.



Extended Data Fig. 4 | Quantification of single-traversal phase coding. a,

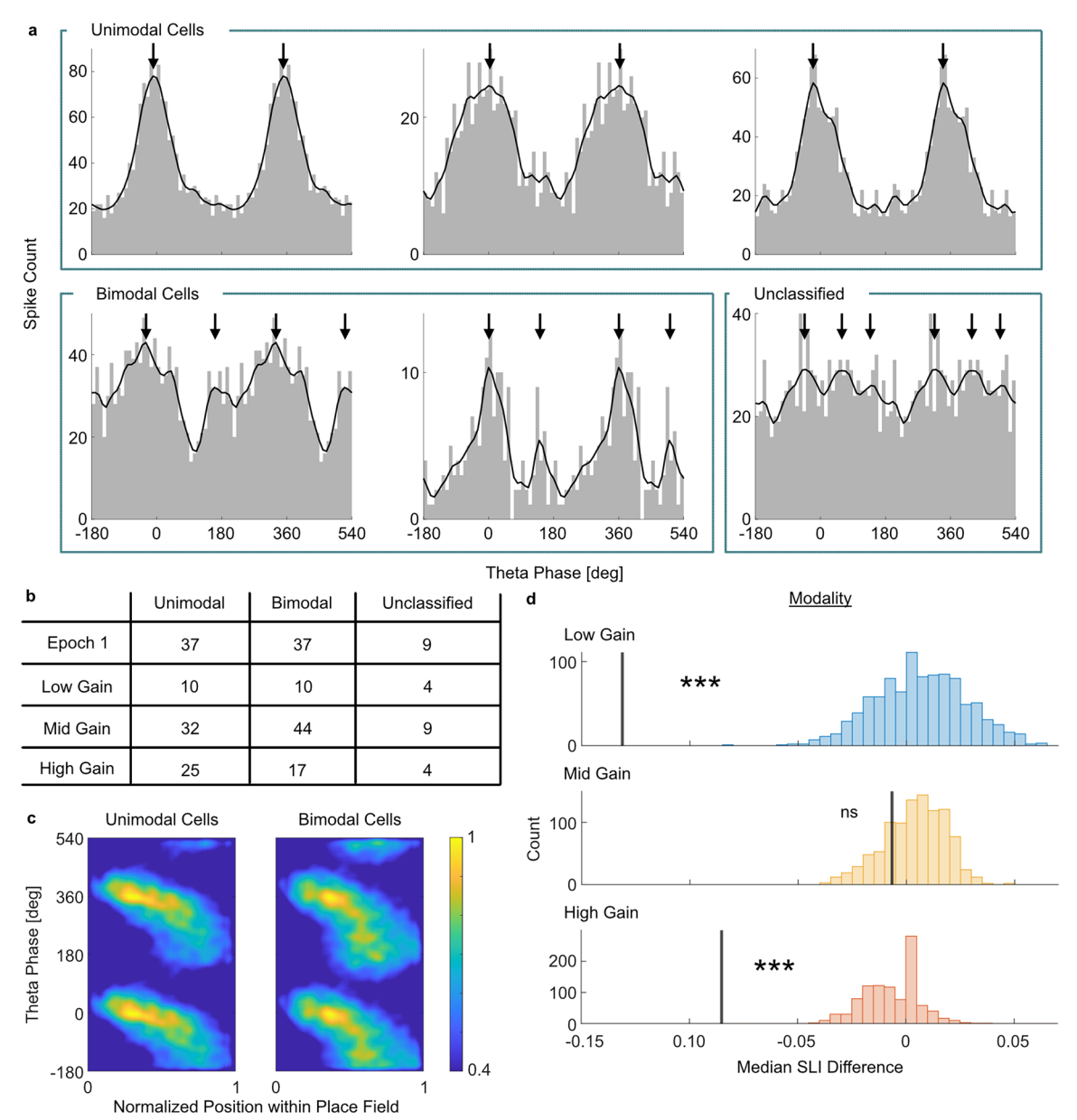
Distribution of single-traversal correlation coefficients. **b**, Distribution of single-traversal phase offsets. **c**, Constant precession can still be fit by a positive slope (red line). The blue-shaded region indicates one theta cycle, with a drop in firing rate in the middle of the field. **d**, Example single-traversal phase coding, fit with half-field slopes. **e**, Proportion of half-field slopes shows the nonmonotonic nature of many single-traversal phase coding. **f**, Proportion of positive half-field slopes. The second half of the field shows increased positive-slope traversals, suggestive of bona fide procession. $\chi^2(1) = 91.97, P = 8.79 \times 10^{-22}$; chi-squared test. **g**, Proportion of positive single-traversal slopes using traversals with strong firing (>= 25 spikes). Overall: $\chi^2(3) = 29.13, P = 2.10 \times 10^{-6}$; Epoch 1 vs. Low: $\chi^2(1) = 18.64, P = 9.46 \times 10^{-5}$, Epoch 1 vs. Mid: $\chi^2(1) = 1.37, P = 0.242$, Epoch 1 vs. High: $\chi^2(1) = 13.66, P = 4.39 \times 10^{-4}$, Low vs. Mid: $\chi^2(1) = 15.45, P = 2.54 \times 10^{-4}$, Low vs. High:

 $\chi^2(1) = 2.13, P = 0.173$, Mid vs. High: $\chi^2(1) = 10.53, P = 1.76 \times 10^{-3}$; chi-squared test followed by FDR correction. **h**, Proportion of positive single-traversal correlation coefficients. Overall: $\chi^2(3) = 41.53, P = 5.05 \times 10^{-9}$; Epoch 1 vs. Low: $\chi^2(1) = 15.54, P = 1.61 \times 10^{-4}$, Epoch 1 vs. Mid: $\chi^2(1) = 2.53, P = 0.112$, Epoch 1 vs. High: $\chi^2(1) = 4.24, P = 0.0474$, Low vs. Mid: $\chi^2(1) = 2.6.90, P = 1.29 \times 10^{-6}$, Low vs. High: $\chi^2(1) = 8.77, P = 4.59 \times 10^{-3}$, Mid vs. High: $\chi^2(1) = 22.80, P = 5.40 \times 10^{-6}$; chi-squared test followed by FDR correction. **i**, Phase offsets of single-traversal phase coding for each gain group. Epoch 1 vs. Low: k(1) = 3.09 \times 104, P = 6.00 \times 10^{-3}, Epoch 1 vs. Mid: k(1) = 1.66 $\times 105, P = 1.50 \times 10^{-3}$, Epoch 1 vs. High: k(1) = 9.12 $\times 104, P = 1.50 \times 10^{-3}$, Mid vs. High: k(1) = 5.78 $\times 105, P = 1.50 \times 10^{-3}$, Low vs. High: k(1) = 7.56 $\times 104, P = 1.50 \times 10^{-3}$, Mid vs. High: k(1) = 5.78 $\times 105, P = 1.50 \times 10^{-3}$; two-sample Kuiper test (two-sided) followed by FDR correction. **j**, Phase occupancy histograms in epoch 4, similar to Fig. 6b. *: P < 0.05, **: P < 0.01, ***: P < 0.001.



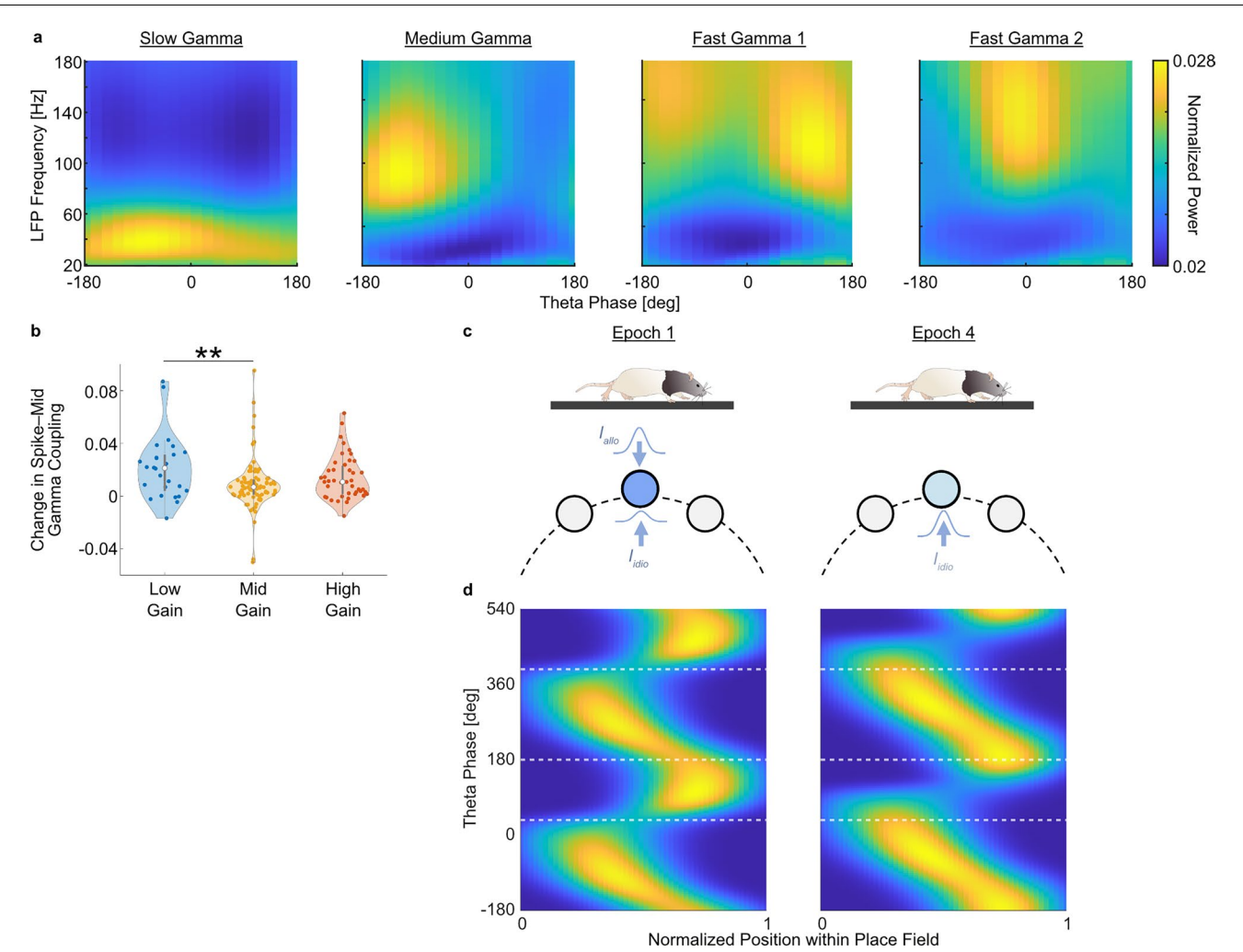
Extended Data Fig. 5 | **Differences in SLIs cannot be explained by other experimental variables. a**, Schematic of the shuffling test based on theta frequency. SLIs in the same theta frequency bins (same color) were shuffled to create a null distribution of SLIs for each gain group. The same procedure was done for the shuffling based on the other parameters. **b**, Shuffling analysis to test if the difference in theta frequency (Fig. 3a) can explain the observed SLIs. The difference in the median SLI compared to epoch 1 was computed and tested against the null distribution. The differences in SLI between epoch 1 and the low and high gain groups were larger than the null distribution, demonstrating that the difference in theta frequency cannot explain the observed effect of SLI. Low: $P <= 1.00 \times 10^{-3}$, Mid: P = 0.249, High: $P <= 1.00 \times 10^{-3}$. **c**, Shuffling analysis to test if the difference in distance traveled by the rat to pass through the field in the lab frame can explain the observed SLIs. The decrease in SLIs in the low and

high gain conditions was greater than the null distribution. Low: $P <= 1.00 \times 10^{-3}$, Mid: P = 0.0870, High: $P <= 1.00 \times 10^{-3}$. **d**, Shuffling analysis to test if the difference in the animal's speed can explain the observed SLIs. The decrease in SLIs in the low and high gain conditions was greater than the null distribution. Low: $P <= 1.00 \times 10^{-3}$, Mid: P = 0.127, High: $P <= 1.00 \times 10^{-3}$. **e**, Shuffling analysis to test if the difference in time since the start of the experiment can explain the observed SLIs. Because epoch 1 is temporally segregated from epoch 3 by definition, shuffling was performed only using epoch 3 data. The decrease in SLIs in the low and high gain conditions compared to the mid gain condition was greater than the null distribution. Low: $P <= 1.00 \times 10^{-3}$, Mid: $P = 8.00 \times 10^{-3}$, High: $P <= 1.00 \times 10^{-3}$. Multiple comparisons correction was not applied for these shuffling analyses. **: P < 0.01, ***: P < 0.001.



Extended Data Fig. 6 | Differences in SLIs cannot be explained by a biased sample of bimodal units. a, Histograms of theta phase preference for example units classified as unimodal, bimodal, and unclassified (>2 peaks) units. Pyramidal cells in the deep layer of CAI tend to exhibit strong firing in both the early and late phases of theta (bimodal cells), while cells in the superficial cell layer tend to fire only in the late phases of theta 37,100 (unimodal cells). X-axis shows the theta phase repeated for two cycles. **b**, Number of units classified in each category. No significant difference in the distribution was observed among gain groups. This finding suggests that gain manipulation affects the relative size of the second lobe while sparing the modality of theta phase preference; for instance, bimodal units maintain their bimodality despite a smaller second lobe

during gain manipulation. $\chi^2(6) = 4.45, P = 0.616$; chi-squared test. **c**, Smoothed phase coding plots for units classified as unimodal and bimodal cells. The plot for the bimodal cells showed a larger second lobe. **d**, Shuffling analysis to test if the difference in the sampling of unit modality can explain the observed SLIs. The decrease in SLIs in the low and high gain conditions was greater than the null distribution. The finding complements that of **b**, together demonstrating that the effect of gain on the size of the second lobe is not due to the change in the theta modality of the units or a biased sampling of unimodal/bimodal units across gain groups. Low: $P <= 1.00 \times 10^{-3}$, Mid: P = 0.229, High: $P <= 1.00 \times 10^{-3}$. Multiple comparisons correction was not applied. ***: P < 0.001.



Extended Data Fig. 7 | Further characterization of the diminishment of the second lobe. a, Slow, medium, and two fast gamma components averaged across sessions. Gamma components were extracted using the unsupervised clustering method of Zhang et al. 103 . The algorithm computed the frequency and the phase power matrix (FPP) for each theta cycle and obtained the groups of pixels in this theta phase–frequency space whose power co-fluctuates across theta cycles using k-mean clustering. The gamma components are coupled to theta phases that match previous studies 68,103,113 . We observed a slow gamma component at a frequency range of -20–60 Hz associated with CA3 inputs (first column) and a medium gamma component at a frequency range of -70–140 Hz associated with MECIII inputs 67,68 (second column). The two fast gamma components (last 2 columns; > -100 Hz) may include spiking artifacts 107 and were not used for further analyses. b, Spike–medium gamma coupling comparison between gains,

limited to the lower half of the medium gamma range (-70-105 Hz) to minimize the overlap in frequency with fast gamma (n = 151 units). Overall: W(2) = 8.78, P = 0.0124 (two-sided); Low vs. Mid: β = 0.0131, s.e. = 4.49 ×10⁻³, t(148) = 2.92, P = 4.01 ×10⁻³, Low vs. High: β = 8.07 ×10⁻³, s.e. = 4.85 ×10⁻³, t(148) = 1.66, P = 0.0985, Mid vs. High: β = -5.07 ×10⁻³, s.e. = 3.70 ×10⁻³, t(148) = -1.37, P = 0.172; Wald test followed by t-statistics/two-sided P values from the LMEM. Each violin plot shows the median (white circle), IQR (gray line), and distribution outline. \mathbf{c} , Conceptual schematics of the network dynamics during epoch 4. In epoch 4, allothetic input is ablated. Note that the idiothetic Gaussian is assigned the larger amplitude (assigned to the allothetic Gaussian in epoch 1), since idiothetic input has the primary control over the hippocampal map in this condition. \mathbf{d} , Position-phase plots of model neurons in epoch 1 and 4. The processing lobe diminished in epoch 4 compared to epoch 1 (same as the middle panel of Fig. 7c).

nature portfolio

Corresponding author(s):	James J. Knierim
Last updated by author(s):	May 12, 2025

Reporting Summary

Nature Portfolio wishes to improve the reproducibility of the work that we publish. This form provides structure for consistency and transparency in reporting. For further information on Nature Portfolio policies, see our <u>Editorial Policies</u> and the <u>Editorial Policy Checklist</u>.

For all statistical analyses, confirm that the following items are present in the figure legend, table legend, main text, or Methods section.

<u> </u>				
۲	· 2	tι	sti	CC

n/a	Confirmed
	\square The exact sample size (n) for each experimental group/condition, given as a discrete number and unit of measurement
	🔀 A statement on whether measurements were taken from distinct samples or whether the same sample was measured repeatedly
	The statistical test(s) used AND whether they are one- or two-sided Only common tests should be described solely by name; describe more complex techniques in the Methods section.
\boxtimes	A description of all covariates tested
	A description of any assumptions or corrections, such as tests of normality and adjustment for multiple comparisons
	A full description of the statistical parameters including central tendency (e.g. means) or other basic estimates (e.g. regression coefficient) AND variation (e.g. standard deviation) or associated estimates of uncertainty (e.g. confidence intervals)
	For null hypothesis testing, the test statistic (e.g. <i>F</i> , <i>t</i> , <i>r</i>) with confidence intervals, effect sizes, degrees of freedom and <i>P</i> value noted <i>Give P values as exact values whenever suitable.</i>
\boxtimes	For Bayesian analysis, information on the choice of priors and Markov chain Monte Carlo settings
\boxtimes	For hierarchical and complex designs, identification of the appropriate level for tests and full reporting of outcomes
	Estimates of effect sizes (e.g. Cohen's <i>d</i> , Pearson's <i>r</i>), indicating how they were calculated
	Our web collection on statistics for biologists contains articles on many of the points above.

Software and code

Policy information about availability of computer code

Data collection

Windows Operating System version 8.1; Ubuntu Linux Operating System versions 12.04, 14.04; Neuralynx Cheetah V5; Robot Operating System (ROS) versions Hydro, Indigo; Xenomai Real-Time Framework versions 2.6, 3.0.

Data analysis

MATLAB version 2023b; Various open-source third-party MATLAB packages from mathworks.org (including k-means clustering); custom WinClust software for spike sorting (written by J. J. Knierim), custom code developed in the study is available via OSF at https://osf.io/nq65k/?.

For manuscripts utilizing custom algorithms or software that are central to the research but not yet described in published literature, software must be made available to editors and reviewers. We strongly encourage code deposition in a community repository (e.g. GitHub). See the Nature Portfolio guidelines for submitting code & software for further information.

Data

Policy information about availability of data

All manuscripts must include a data availability statement. This statement should provide the following information, where applicable:

- Accession codes, unique identifiers, or web links for publicly available datasets
- A description of any restrictions on data availability
- For clinical datasets or third party data, please ensure that the statement adheres to our policy

Preprocessed data used to perform the analyses and generate the figures in this manuscript is publicly available via OSF at https://osf.io/nq65k/?.

Research involving human participants, their data, or biological material

Policy information about studies with <u>human participants or human data</u> . See also policy information about <u>sex, gender (identity/presentation),</u>	
and sexual orientation and race, ethnicity and racism.	

Reporting on sex and gender	n/a
Reporting on race, ethnicity, or other socially relevant groupings	n/a
Population characteristics	n/a
Recruitment	n/a
Ethics oversight	n/a

Note that full information on the approval of the study protocol must also be provided in the manuscript.

Field-specific reporting

For a reference copy of the document with all sections, see <u>nature.com/documents/nr-reporting-summary-flat.pdf</u>

Life sciences study design

All studies must disclose on these points even when the disclosure is negative.

Sample size

No statistical methods were used to pre-determine sample size in these exploratory studies. The number of animals (n = 5) was determined based on standards used to established results in other peer-reviewed publications in the field (e.g., Jayakumar, Madhav, et al., 2019; Hockeimer et al., 2025). The number of sessions per animal varied based onbehavioral state, number of units being recorded and observed stability of recordings.

Data exclusions

Sessions were excluded from analysis if they did not meet all of the following criteria. Criteria 1-4 are standard for our lab and were preestablished. Criteria 5-6 were specific for this experiment, not pre-established but were used to ensure that the session provided data of sufficient quality to address the experimental question. None of the exclusion criteria affected or biased the experimental results. (1) There were no experimental disruptions, such as too much manual intervention during the session or too many long breaks in recording due to behavioral performance or technical issues. (2) At least one unit deemed 'fair' or above, according to our manual quantification of cluster isolation quality. (3) At least one unit having more than 50 spikes during the session that fired when the animal ran at a velocity of more than 5 cm/s. (4) At least one unit classified as a putative pyramidal cell, using our classification based on mean firing rate, spike width, and typical ISI. (5). The rat ran at least 12 laps in the session with landmarks on. (6) Our population decoding method was able to provide a population hippocampal gain estimate for at least half of the duration while the landmarks were on.

Replication

The dataset consisted of data from five different individual rats that all showed landmark control of the place cells and subsequent recalibration of path integration gain. For each animal, each gain was replicated twice, but the results were included for analysis only if the behavior of the animal allowed the completion of the experiment. In most cases, the same gain resulted in qualitatively identical results (landmark control or landmark failure). In some cases, the visual landmarks lost control over the hippocampal map at a gain that had control in a previous session; the observation aligns with the understanding that landmarks that are deemed unstable by the animal from previous sessions would show weaker control of the place field map in the subsequent sessions. Analyses of individual rats are presented when applicable. There have been no indications that would prevent replication of these results, except the emergence of failure of control of the hippocampal place fields by landmarks. Since this happens upon repeated exposure to moving landmark cues especially in gains further from 1, care must be taken to avoid excessive/abrupt landmark manipulation while replicating these results.

Randomization

There were no experimental groups for the subjects, since we ran similar sessions on all five animals used in this study.

Blinding

The investigators were not blind to the identity of the animal or the experimental gain being applied during data collection, since the experiments had to monitor the VR system to ensure proper functionality and and intervene when necessary. Isolation and classification of clusters, however, was done blind to the experimental manipulation being applied. The data analysis software was also blind to the parameters of the trial.

Reporting for specific materials, systems and methods

We require information from authors about some types of materials, experimental systems and methods used in many studies. Here, indicate whether each material, system or method listed is relevant to your study. If you are not sure if a list item applies to your research, read the appropriate section before selecting a response.

Materials & experime	ntal systems Methods
n/a Involved in the study	n/a Involved in the study
Antibodies	ChIP-seq
Eukaryotic cell lines	Flow cytometry
Palaeontology and a	archaeology MRI-based neuroimaging
Animals and other of	organisms
Clinical data	
Dual use research o	f concern
Animals and othe	r research organisms
Policy information about <u>st</u> <u>Research</u>	udies involving animals; ARRIVE guidelines recommended for reporting animal research, and Sex and Gender in
Laboratory animals	Rattus norvegicus, Long Evans, 5-8 months old, 300-450 g. weight
Wild animals	No wild animals were used in this study.
Reporting on sex	This work analyzes a previously published dataset that consisted of five male animals. The composition of sex follows the field standard at the time when the original data was collected.
Field-collected samples	No field-collected samples were used in this study.
Ethics oversight	All animal care and housing procedures complied with National Institutes of Health guidelines and followed protocols approved by the Institutional Animal Care and Use Committee at Johns Hopkins University.
Note that full information on t	he approval of the study protocol must also be provided in the manuscript.
Plants	
Seed stocks	n/a
Novel plant genotypes	n/a
Authentication	n/a